MULTISCALE MODEL. SIMUL.
Vol. 22, No. 4, pp. 1326–1364

POTENTIAL SINGULARITY OF THE AXISYMMETRIC EULER EQUATIONS WITH C^α INITIAL VORTICITY FOR A LARGE RANGE OF α^*

THOMAS Y. HOU† AND SHUMAO ZHANG†

Abstract. We provide numerical evidence for a potential finite-time self-similar singularity of the three-dimensional (3D) axisymmetric Euler equations with no swirl and with C^α initial vorticity for a large range of α. We employ a highly effective adaptive mesh method to resolve the potential singularity sufficiently close to the potential blow-up time. Resolution study shows that our numerical method is at least second-order accurate. Scaling analysis and the dynamic rescaling method are presented to quantitatively study the scaling properties of the potential singularity. We demonstrate that this potential blow-up is stable with respect to the perturbation of initial data. Our numerical study shows that the 3D axisymmetric Euler equations with our initial data develop finite-time blow-up when the Hölder exponent α is smaller than some critical value α^*, which has the potential to be 1/3. We also study the n-dimensional axisymmetric Euler equations with no swirl, and observe that the critical Hölder exponent α^* is close to $1-\frac{2}{n}$. Compared with Elgindi's blow-up result in a similar setting [T. M. Elgindi, *Ann. of Math.*, 194 (2021), pp. 647–727], our potential blow-up scenario has a different Hölder continuity property in the initial data and the scaling properties of the two initial data are also quite different. We also propose a relatively simple one-dimensional model and numerically verify its approximation to the n-dimensional axisymmetric Euler equations. This one-dimensional model sheds useful light to our understanding of the blow-up mechanism for the n-dimensional Euler equations.

Key words. 3D axisymmetric Euler equations, finite-time blow-up

MSC codes. 35Q31, 76B03, 65M60, 65M06, 65M20

DOI. 10.1137/22M1542453

1. Introduction.

The three-dimensional (3D) incompressible Euler equations in fluid dynamics describe the motion of inviscid incompressible flows and are one of the most fundamental equations in fluid dynamics. Despite their wide range of applications, the question regarding the global regularity of the Euler equations has been widely recognized as a major open problem in partial differential equations (PDEs) and is closely related to the Millennium Prize Problem on the Navier–Stokes equations listed by the Clay Mathematics Institute [22]. In 2014, Luo and Hou [41, 42] considered the 3D axisymmetric Euler equations with smooth initial data and boundary, and presented strong numerical evidences that they can develop potential finite-time singularity. The presence of the boundary, the symmetry properties, and the direction of the flow in the initial data collaborate with each other in the formation of a sustainable finite-time singularity. Recently, Chen and Hou [7, 8] provided a rigorous justification of the Luo-Hou blow-up scenario.

In 2021, Elgindi [20] showed that given appropriate C^α initial vorticity with $\alpha > 0$ sufficiently small, the 3D axisymmetric Euler equations with no swirl can develop finite-time singularity. In Elgindi's work, the initial data for the vorticity ω have C^α

*Received by the editors December 22, 2022; accepted for publication (in revised form) June 21, 2024; published electronically October 8, 2024.
https://doi.org/10.1137/22M1542453
Funding: The research was supported in part by DMS-2205590. We would like to acknowledge the generous support from Mr. K. C. Choi through the Choi Family Gift Fund and the Choi Family Postdoc Gift Fund.
†Department of Computing and Mathematical Sciences, California Institute of Technology, Pasadena, CA 91125 USA (hou@cms.caltech.edu, shumaoz@caltech.edu).

Hölder continuity near $r=0$ and $z=0$. When α is small enough, Elgindi approximated the 3D axisymmetric Euler equations by a fundamental model that develops a self-similar finite-time singularity. The blow-up result obtained in [20] has infinite energy. In a subsequent paper [18], the authors improved the result obtained in [20] to have finite energy blow-up.

In this work we study potential finite-time singularity of the 3D axisymmetric Euler equations with no swirl and C^α initial vorticity for a large range of α. Define $\omega = \nabla \times u$ as the vorticity vector, and then the 3D incompressible Euler equations can be written in the vorticity stream function formulation:

$$\begin{aligned} \omega_t + u\cdot\nabla\omega &= \omega\cdot\nabla u, \\ -\nabla\psi &= \omega, \\ u &= \nabla\times\psi, \end{aligned} \tag{1.1}$$

where ψ is the vector-valued stream function. Let us use $x=(x_1,x_2,x_3)$ to denote a point in $\mathbb{R}^3$, and let e_r, e_θ, e_z be the unit vectors of the cylindrical coordinate system

$$e_r = (x_1/r, x_2/r, 0)\,, \quad e_\theta = (x_2/r, -x_1/r, 0)\,, \quad e_z = (0,0,1)\,,$$

where $r=\sqrt{x_1^2+x_2^2}$ and $z=x_3$. We say a vector field v is axisymmetric if it admits the decomposition

$$v = v^r(r,z)e_r + v^\theta(r,z)e_\theta + v^z(r,z)e_z,$$

namely, v^r, v^θ, and v^z are independent of the angular variable θ. Denote by u^θ, ω^θ, and ψ^θ the angular velocity, vorticity, and stream function, respectively. The axisymmetric condition can then simplify the 3D Euler equations (1.1) to [44]:

$$u^\theta_t + u^r u^\theta_r + u^z u^\theta_z = -\frac{1}{r}u^r u^\theta, \tag{1.2a}$$

$$\omega^\theta_t + u^r\omega^\theta_r + u^z\omega^\theta_z = \frac{2}{r}u^\theta u^\theta_z + \frac{1}{r}u^r\omega^\theta, \tag{1.2b}$$

$$-\psi^\theta_{rr} - \psi^\theta_{zz} - \frac{1}{r}\psi^\theta_r + \frac{1}{r^2}\psi^\theta = \omega^\theta, \tag{1.2c}$$

$$u^r = -\psi^\theta_z, \quad u^z = \frac{1}{r}\psi^\theta + \psi^\theta_r. \tag{1.2d}$$

In the case of no swirl, i.e., $u^\theta \equiv 0$, the axisymmetric Euler equations are further simplified into

$$\omega^\theta_t + u^r\omega^\theta_r + u^z\omega^\theta_z = \frac{1}{r}u^r\omega^\theta, \tag{1.3a}$$

$$-\psi^\theta_{rr} - \psi^\theta_{zz} - \frac{1}{r}\psi^\theta_r + \frac{1}{r^2}\psi^\theta = \omega^\theta, \tag{1.3b}$$

$$u^r = -\psi^\theta_z, \quad u^z = \frac{1}{r}\psi^\theta + \psi^\theta_r. \tag{1.3c}$$

When the initial condition for the angular vorticity ω^θ is smooth, it is well known that the 3D axisymmetric Euler equations with no swirl (1.3) will not develop finite-time blow-up [54]. Therefore, we consider (1.3) when the initial condition for the angular vorticity ω^θ is C^α Hölder continuous for a large range of α. By using an effective adaptive mesh method, we will provide convincing numerical evidence that the 3D axisymmetric Euler equations with no swirl and C^α initial voriticity with α greater

than or equal to 0, and smaller than some critical value α^* can develop potential finite-time self-similar blow-up. The critical Hölder exponent α^* is observed to be larger than 0.3 and close to 1/3. Our result serves as an example to support Conjecture 8 of [18] that the critical value α^* is equal to 1/3.

We perform scaling analysis and use the dynamic rescaling formulation [27, 6, 9] to study the behavior of the potential self-similar blow-up. An operator splitting method is proposed to solve the dynamic rescaling formulation and the late time solution from the adaptive mesh method is used as our initial condition for the dynamic rescaling formulation. We observe rapid convergence to a steady state, which implies that this potential singularity is self-similar. We notice that the size of the finite computational domain needs to be large enough to approximate steady state, due to a scale-invariant property of the dynamic rescaling equation. So we conduct domain size study to verify the accuracy of our results. We will also demonstrate that this potential blow-up is stable with respect to the perturbation of initial data, suggesting that the underlying blow-up mechanism is generic and insensitive to the initial data.

We choose the following C^α initial data for the angular vorticity ω^θ:

$$\omega_0^\theta = \frac{-12000\, r^\alpha \left(1-r^2\right)^{18} \sin(2\pi z)}{1+12.5\cos^2(\pi z)}.$$

The initial condition is a smooth and periodic function in z and is C^α in r. The velocity field u becomes $C^{1,\alpha}$ continuous. We further introduce the new variables:

$$\omega_1(r,z) = \frac{1}{r^\alpha}\omega^\theta(r,z), \quad \psi_1(r,z) = \frac{1}{r}\psi^\theta(r,z), \tag{1.4}$$

to remove the formal singularity in (1.3) near $r = 0$. In terms of the new variables (ω_1, ψ_1), the 3D axisymmetric Euler equations with no swirl have the following equivalent form:

$$\omega_{1,t} + u^r\omega_{1,r} + u^z\omega_{1,z} = -(1-\alpha)\psi_{1,z}\omega_1, \tag{1.5a}$$

$$-\psi_{1,rr} - \psi_{1,zz} - \frac{3}{r}\psi_{1,r} = \omega_1 r^{\alpha-1}, \tag{1.5b}$$

$$u^r = -r\psi_{1,z}, \quad u^z = 2\psi_1 + r\psi_{1,r}. \tag{1.5c}$$

The above reformulation is crucial for us to perform accurate numerical computation of the potential singular solution and allow us to push the computation sufficiently close to the singularity time.

It is important to note that the initial condition for the rescaled vorticity field ω_1 is a smooth function of r and z. Using the above reformulation enables us to resolve the potential singular solution sufficiently close to the potential singularity time. If we solve the original 3D Euler equations (1.3a)–(1.3c), it is extremely difficult to resolve the Hölder continuous vorticity even with an adaptive mesh, especially for small α. For this reason, we have not been able to compute the finite-time singularity in Elgindi's work [20] since such a reformulation is not available for his initial data.

Compared with Elgindi's blow-up result [20], our potential blow-up scenario has very different scaling properties. In our scenario, the scaling factor c_l, defined in (2.6), increases with α and tends to infinity as α approaches α^*; see Table 4. In contrast, the scaling factor c_l in Elgindi's scenario is $1/\alpha$, which decreases with α and tends to infinity as α approaches 0. Another difference is that Elgindi's initial vorticity is $C^{2\alpha}$ in r and C^α in z near the origin, while our initial vorticity is C^α in r, but smooth in z. We discuss the comparison in details in section 7.

We also consider the n-dimensional axisymmetric Euler equations (see definitions in (5.3)). We observe the same potential self-similar finite-time blow-up and find that the critical value α^* is close to $1-\frac{2}{n}$. The self-similar profiles for high-dimensional Euler equations are qualitatively similar to those of the 3D Euler equations. We observe that the blow-up is more robust for higher space dimensions and the scaling factor c_l decreases as n increases, which may be partially due to the stronger nonlinearity in the vortex stretching term with larger n. Similar to the 3D Euler equations, we see c_l quickly increases with α, and has the trend to go to infinity as $\alpha \to \alpha^*$. We observe that the stream function ψ_1 becomes almost linear in the near field along the rescaled z variable (denoted as ζ) as $\alpha \to \alpha^*$. Another interesting observation is that ω_1 becomes increasingly flat as a function of the rescaled r variable ξ. Based on this observation, we propose a simplified one-dimensional (1D) model along the z-direction by extending ω_1 as a constant in the r-direction. This is equivalent to approximating $\omega^\theta(r,z,t) \approx r^\alpha \omega_1(0,z,t)$, which still captures the effect of the Hölder continuity of ω^θ through r^α. Although this 1D model is supposed to give a good approximation of the 3D Euler equation as $\alpha \to \alpha^*$, we also observe that it can approximate the self-similar profile of the 3D Euler equation along the z-axis and its scaling factor c_l very well even for small α. The analysis of the 1D model should shed useful light on the blow-up mechanism of the 3D and the n-D Euler equations.

There has been exciting recent progress on the global regularity of the high-dimensional axisymmetric Euler equations with no swirl with smooth initial data under some assumptions; see, e.g., [12, 46, 37]. In particular, when $n=4$, Choi, Jeong, and Lim [12] proved global regularity of the four-dimensional (4D) axisymmetric Euler equation with no swirl under the assumption that the initial vorticity satisfies some decay condition at infinity and is vanishing at the symmetry axis. Further, if the initial vorticity is of one sign, they proved global regularity for $n \le 7$. This result is further improved in a subsequent paper by Lim [37] to any dimension $n \ge 4$ under a similar decay assumption and for one-signed vorticity. In [46], Miller showed that the four- and higher-dimensional axisymmetric Euler equations with no swirl have properties which could lead to finite-time blow-up that is excluded for the 3D Euler equation. The author also considered a model for the infinite-dimensional vorticity equation, which exhibits finite-time blow-up of a Burgers shock type. The blow-up result of this model equation seems to suggest that the Euler equation in sufficiently high dimension is likely to develop a finite-time blow-up with smooth initial data.

In an excellent survey paper by Drivas and Elgindi [18], the authors discussed singularity formation in the high-dimensional incompressible Euler equation in some details. In particular, the authors asked in their Open Question 7 that if singularities can form from smooth data for the axisymmetric no-swirl Euler equations on $\mathbb{R}^n$ when $n \ge 4$. To the best of our knowledge, there has been no strong numerical evidence for potential finite-time blow-up for the n-dimensional axisymmetric Euler equation with no swirl and smooth initial data. We have performed such computation by ourselves and did not find any evidence for finite-time blow-up. One of the reasons for the non-blow-up is that the quantity ω^θ/r^{n-2} satisfies a transport equation with no vortex stretching, thus ω^θ/r^{n-2} satisfies a maximum principle. As long as ω^θ/r^{n-2} is well defined at $t=0$ and ω^θ decays rapidly at infinity, we will have control of the maximum growth of vorticity, thus there is no finite-time blow-up [12, 46, 37].

Theoretical analysis of the 3D Euler equations have been studied for a long time. The Beale–Kato–Majda (BKM) blow-up criterion [2, 23] gives a necessary and sufficient condition for the finite-time singularity for the smooth solutions of the 3D Euler equations at time T if and only if $\int_0^T \|\omega(\cdot,t)\|_{L^\infty} \mathrm{d}t = +\infty$. This result also holds true

for Hölder continuous initial data (see Theorem 4.3 of [44]) and can be easily generalized to high-dimensional Euler equations. In [13], Constantin, Fefferman, and Majda asserted that there will be no finite-time blow-up if the velocity u is uniformly bounded and the direction of vorticity $\xi = \omega/|\omega|$ is sufficiently regular (Lipschitz continuous) in an $O(1)$ domain containing the location of the maximum vorticity. Inspired by the work of [13], Deng, Hou, and Yu developed a more localized non-blow-up criterion using a Lagrangian approach in [17].

There have been a number of numerical attempts in search of the potential finite-time blow-up. The finite-time blow-up in the numerical study was first reported by Grauer and Sideris [25] and Pumir and Siggia [48] for the 3D axisymmetric Euler equations. However, the later work of E and Shu [19] suggested that the finite-time blow-up in [25, 48] could be caused by numerical artifact. Kerr and his collaborators [29, 3] presented finite-time singularity formation in the Euler flows generated by a pair of perturbed antiparallel vortex tubes. In [28], Hou and Li reproduced Kerr's computation using a similar initial condition with much higher resolutions and did not observe finite-time blow-up. The maximum vorticity grows slightly slower than double exponential in time. Later, Kerr confirmed in [30] that the solutions from [29] eventually converge to a superexponential growth and are unlikely to lead to a finite-time singularity.

In [4, 52], Caflisch and his collaborators studied axisymmetric Euler flows with complex initial data and reported singularity formation in the complex plane. The review paper [24] lists a more comprehensive collection of interesting numerical results with more detailed discussions.

Due to the lack of stable structure in the potentially singular solutions, the previously mentioned numerical results remain inconclusive. In [41, 42], Luo and Hou reported that the 3D axisymmetric Euler equations with a smooth initial condition developed a self-similar finite-time blow-up in the meridian plane on the boundary of $r = 1$; see also [43]. The Hou–Luo blow-up scenario has generated a great deal of interest in both the mathematics and fluid dynamics communities, and inspired a number of subsequent developments [33, 32, 31, 11, 10, 6, 9, 7, 8, 15, 14, 5].

We remark that there has been recent exciting progress on the theoretical study of singularity formation of the two-dimensional (2D) Boussinesq system and the 3D Euler equations. In [21], Elgindi and Pasqualotto established finite-time singularity formation for $C^{1,\alpha}$ solutions to the Boussinesq system that are compactly supported on $\mathbb{R}^2$ and infinitely smooth except in the radial direction at the origin. In [15], Cordoba, Martinez-Zorao, and Zheng constructed non-self-similar blow-up solutions of the 3D axisymmetric Euler equation with no swirl and C^α initial vorticity, which is smooth except at the origin. Inspired by the work of [15], Chen in [5] showed that Elgindi's $C^{1,\alpha}$ self-similar blow-up can be improved to be smooth except at the origin. Further, Cordoba and Martinez-Zorao constructed finite-time singularity of 3D incompressible Euler equations with velocity in $C^{3,1/2} \cap L^2$ and uniform $C^{1,1/2-\epsilon} \cap L^2$ force.

The rest of this paper is organized as follows. In section 2, we briefly introduce the numerical method. We present the evidence of the potential self-similar blow-up in section 3, and provide the resolution study and scaling analysis for the case of $\alpha = 0.1$. In section 4 we use the dynamic rescaling method to provide further evidence of the potential blow-up. In section 5, we consider the potential finite-time blow-up in the general case of the Hölder exponent α and the dimension n. The sensitivity of the potential blow-up to the initial data is considered in section 6, and the comparison of our potential blow-up scenario with Elgindi's scenario in [20] is discussed in section 7. Section 8 is devoted to a 1D model to study the potential self-similar blow-up of the

n-dimensional axisymmetric Euler equations. Some concluding remarks are made in section 9.

2. Problem set up and numerical method. In this section, we give details about the setup of the problem, the initial data, the boundary conditions, and some basic properties of the equations, and our numerical method.

2.1. Boundary conditions and symmetries. We consider (1.5) in a cylinder region

$$\mathcal{D}_{\text{cyl}} = \{(r,z) : 0 \le r \le 1\}.$$

We impose a periodic boundary condition in z with period 1:

$$\omega_1(r,z) = \omega_1(r,z+1), \quad \psi_1(r,z) = \psi_1(r,z+1). \tag{2.1}$$

In addition, we enforce that (ω_1, ψ_1) are odd in z at $z = 0$:

$$\omega_1(r,z) = -\omega_1(r,-z), \quad \psi_1(r,z) = -\psi_1(r,-z). \tag{2.2}$$

And this symmetry will be preserved dynamically by the 3D Euler equations.

At $r = 0$, it is easy to see that $u^r(0,z) = 0$, so there is no need for the boundary condition for ω_1 at $r = 0$. Since $\psi^\theta = r\psi_1$ will at least be C^2-continuous, according to [38, 39], ψ^θ must be an odd function of r. Therefore, we impose the following pole condition for ψ_1:

$$\psi_{1,r}(0,z) = 0. \tag{2.3}$$

We impose the no-flow boundary condition at the boundary $r = 1$:

$$\psi_1(1,z) = 0. \tag{2.4}$$

This implies that $u^r(1,z) = 0$. So there is no need to introduce a boundary condition for ω_1 at $r = 1$.

Due to the periodicity and the odd symmetry along the z-direction, (1.3) need only be solved on the half-periodic cylinder

$$\mathcal{D} = \{(r,z) : 0 \le r \le 1, 0 \le z \le 1/2\}.$$

The above boundary conditions of $\mathcal{D}$ show that there is no transport of the flow across its boundaries. Indeed, we have

$$u^r = 0 \quad \text{on} \quad r = 0 \text{ or } 1, \quad \text{and} \quad u^z = 0 \quad \text{on} \quad z = 0 \text{ or } 1/2.$$

Thus, the boundaries of $\mathcal{D}$ behave like "impermeable walls".

2.2. Initial data. Inspired by the potential blow-up scenario in [26], we propose the following initial data for ω_1 in $\mathcal{D}$:

$$\omega_1^\circ = \frac{-12000\left(1-r^2\right)^{18}\sin(2\pi z)}{1+12.5\cos^2(\pi z)}. \tag{2.5}$$

Later, we will see in section 6 that the self-similar singularity formation has some robustness to the choice of initial data. We solve the Poisson equation (1.5b) to get the initial value ψ_1° of ψ_1.

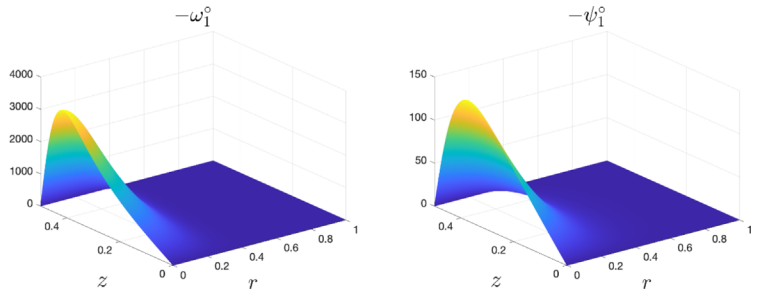

FIG. 1. *3D profiles of the initial value* $-\omega_1^\circ$ *and* $-\psi_1^\circ$.

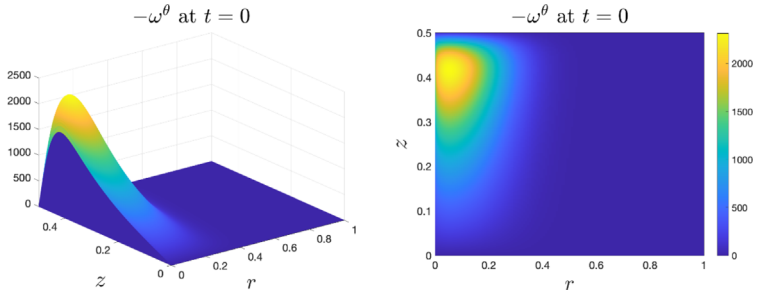

FIG. 2. *The initial data for the angular vorticity* ω^θ.

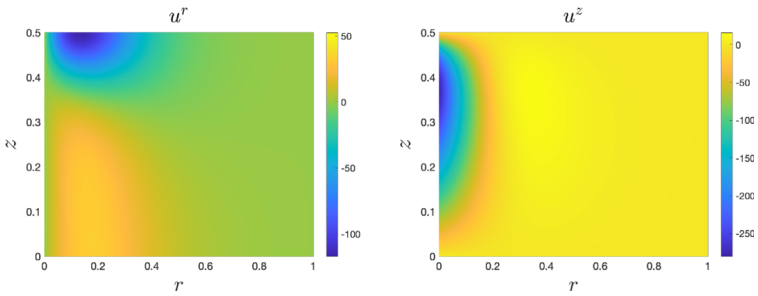

FIG. 3. *Initial velocity fields* u^r *and* u^z.

The 3D profiles of $(\omega_1^\circ, \psi_1^\circ)$ can be found in Figure 1. Since most parts of ω_1° and ψ_1° are negative, we negate them for better visual effect when generating figures. In Figure 2, we show the 3D profile and pseudocolor plot of the angular vorticity ω^θ at $t=0$. We can see that there is a sharp drop to zero of $-\omega^\theta$ near $r=0$, which is due to the Hölder continuous of ω^θ at $r=0$.

We plot the initial velocity fields u^r and u^z in Figure 3. We can see that u^r is primarily positive near $z=0$ and negative near $z=1/2$ when r is small, and u^z is mainly negative when r is small. Such a pattern suggests a hyperbolic flow near $(r,z)=(0,0)$ as depicted in the heuristic diagram Figure 4, which will extend periodically in z.

2.3. Self-similar solution. Self-similar solutions are a common and important class of solutions to nonlinear PDEs that demonstrate their intrinsic structure and properties. A self-similar solution is when the local profile of the solution remains

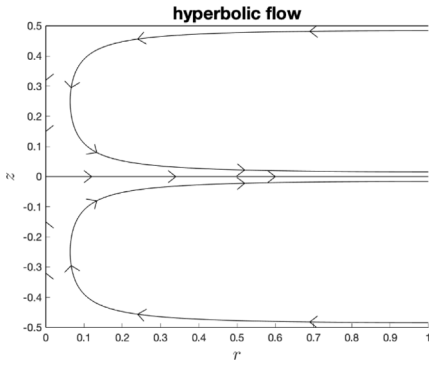

FIG. 4. *A heuristic diagram of the hyperbolic flow.*

nearly unchanged in time after rescaling the spatial and the temporal variables of the physical solution. For example, for (1.5), the self-similar profile is the ansatz

$$\begin{aligned} \omega_1(x,t) &\approx \frac{1}{(T-t)^{c_\omega}}\Omega\left(\frac{x-x_0}{(T-t)^{c_l}}\right), \\ \psi_1(x,t) &\approx \frac{1}{(T-t)^{c_\psi}}\Psi\left(\frac{x-x_0}{(T-t)^{c_l}}\right), \end{aligned} \tag{2.6}$$

for some parameters c_ω, c_ψ, c_l, x_0, and T. Here T is considered as the blow-up time, and x_0 is the location of the self-similar blow-up. The parameters c_ω, c_ψ, c_l are called scaling factors.

It is also important to notice that the 3D Euler equations (1.1) enjoy the following scaling invariant property: if (u,ω,ψ) is a solution to (1.1), then $(u_{\lambda,\mu},\omega_{\lambda,\mu},\psi_{\lambda,\mu})$ is also a solution, where

$$u_{\lambda,\mu}(x,t)=\frac{\lambda}{\mu}u\left(\frac{x}{\lambda},\frac{t}{\mu}\right), \quad \omega_{\lambda,\mu}(x,t)=\frac{1}{\mu}\omega\left(\frac{x}{\lambda},\frac{t}{\mu}\right), \quad \psi_{\lambda,\mu}(x,t)=\frac{\lambda^2}{\mu}\psi\left(\frac{x}{\lambda},\frac{t}{\mu}\right),$$

and $\lambda>0$, $\mu>0$ are two constant scaling factors. In the case of the 3D axisymmetric Euler equations with no swirl (1.5), the scaling invariant property can be equivalently translated to the following: if (ω_1,ψ_1) is a solution of (1.5), then

$$\left\{\frac{1}{\lambda^\alpha\mu}\omega_1\left(\frac{x}{\lambda},\frac{t}{\mu}\right),\ \frac{\lambda}{\mu}\psi_1\left(\frac{x}{\lambda},\frac{t}{\mu}\right)\right\} \tag{2.7}$$

is also a solution.

If we assume the existence of the self-similar solution (2.6), then the new solutions in (2.7) should also admit the same ansatz, regardless of the values of λ and μ. As a result, we must have

$$c_\omega=1+\alpha c_l, \quad c_\psi=1-c_l. \tag{2.8}$$

Therefore, the self-similar profile (2.7) of (1.5) only has one degree of freedom, for example c_l, in the scaling factors. In fact, c_l cannot be determined by straightforward dimensional analysis.

As a consequence of the ansatz (2.6) and the scaling relation (2.8), we have

$$\|\omega^\theta(x,t)\|_{L^\infty}\sim\frac{1}{T-t}, \quad \|\psi_{1,z}(x,t)\|_{L^\infty}\sim\frac{1}{T-t}, \tag{2.9}$$

which always holds true regardless of the value of c_l.

2.4. Numerical method. Although the initial data are very smooth, the solutions of Euler equations quickly become very singular and concentrate in a rapidly shrinking region. Therefore, we use the adaptive mesh method to resolve the singular profile of the solutions. A detailed description of the adaptive mesh method can be found in [27, 43, 55]. Here we briefly introduce the idea behind the adaptive mesh method. The specific parameter setting used for the experiments in this work can be found in the appendix of [55].

The Euler equations (1.5) are originally posted as an initial-boundary value problem on the computational domain $(r,z) \in [0,1] \times [0,1/2]$. To capture the singular part of the solution, we introduce two variables $(\kappa,\eta) \in [0,1] \times [0,1]$, and the maps

$$r = r(\kappa), \quad z = z(\eta),$$

where we assume these two maps and their derivatives are all analytically known. We update these two maps from time to time according to some criteria and construct these two maps as monotonically increasing functions. We will use these two maps to map the physical domain in (r,z) to a computational domain in (κ,η), so that $\omega_1(r(\kappa),z(\eta))$ and $\psi_1(r(\kappa),z(\eta))$ as functions of (κ,η) are relatively smooth. Let n_κ, n_η be the number of grid points along the r- and z- directions, respectively. And let $h_\kappa = 1/n_\kappa$, $h_\eta = 1/n_\eta$ be the mesh sizes along the r- and z-directions, respectively. We place a uniform mesh on the computation domain of (κ,η):

$$\mathcal{M}_{(\kappa,\eta)} = \{(ih_\kappa, jh_\eta) : 0 \le i \le n_\kappa, 0 \le j \le n_\eta\}.$$

This is equivalent to covering the physical domain of (r,z) with the tensor-product mesh:

$$\mathcal{M}_{(r,z)} = \{(r(ih_\kappa), z(jh_\eta)) : 0 \le i \le n_\kappa, 0 \le j \le n_\eta\}.$$

With properly chosen maps of $r = r(\kappa)$ and $z = z(\eta)$, the mesh $\mathcal{M}_{(r,z)}$ can focus on the singular part of the solution, so that the accuracy of the numerical solution can be greatly improved.

As we will see in the following sections, the singular part of the solutions will gradually move towards the origin. Thus we dynamically update the maps to accommodate the movement of the focused region. The update of the maps is based on an adaptive strategy that quantitatively locates the singular part of the solution and then decides the necessity to change the maps, as well as the parameters for the new maps. Once we update the maps, we interpolate the solutions from the old mesh to the new mesh and use the new computational domain. In our algorithm, we adopt a second-order implementation for our adaptive mesh method. In section 3.3, we will perform resolution study to confirm the order of accuracy of our numerical method.

3. Numerical evidence for a potential self-similar singularity. In this section, we will focus on the case with Hölder exponent $\alpha = 0.1$, and provide numerical evidences for the potential self-similar singularity observed from the 3D axisymmetric Euler equations with no swirl and with Hölder continuous initial data. For the cases with different values of Hölder exponent α, we will present the results in section 5.

3.1. Evidence for a potential singularity. On 1024×1024 spatial resolution, we use the adaptive mesh method to solve (1.5) with Hölder exponent $\alpha = 0.1$, until the time when the smallest adaptive mesh size gets close to the machine precision. The final time of the computation is at $t = 1.6524635 \times 10^{-3}$, after more than 6.5×10^4 iterations in time.

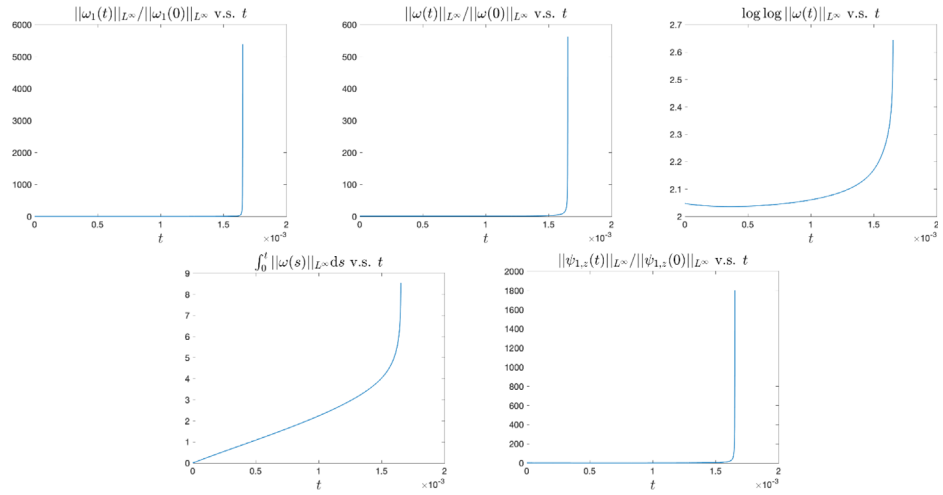

FIG. 5. *Curves of* $\|\omega_1\|_{L^\infty}$, $\|\omega\|_{L^\infty}$, $\log\log\|\omega\|_{L^\infty}$, $\int_0^t \|\omega(s)\|_{L^\infty} ds$, $\|\psi_{1,z}\|_{L^\infty}$ *as functions of time* t.

In Figure 5, we plot the dynamic growth of several important quantities of the solution. The magnitude of ω_1 has grown significantly, especially near the end of the computation. At the final time of the computation, $\|\omega_1\|_{L^\infty}$ has increased by a factor of around 5400, and $\|\omega\|_{L^\infty}$ has increased by a factor of more than 560. We also observe that the double logarithm curve of the maximum vorticity magnitude, $\log\log\|\omega\|_{L^\infty}$, maintains a superlinear growth, and the time integral $\int_0^t \|\omega(s)\|_{L^\infty} ds$ has rapid growth with strong growth inertia close to the stopping time. This provides strong evidence for a potential finite-time blow-up of the 3D Euler equations by the BKM blow-up criterion. We see rapid increase in $\|\psi_{1,z}\|_{L^\infty}$ in time, which shows very strong vortex stretching term $-(n-2-\alpha)\psi_{1,z}\omega_1$ near the potential finite-time blow-up. We analyze their scaling time t in section 3.4.

In Figure 6, we plot the 3D profiles of ω_1, ψ_1, ω^θ, ψ^θ, u^r, and u^z near the origin at the end of our computation. We can see that ω_1 is very concentrated near the origin, and so is ω^θ. Therefore, we further zoom-in around the origin and plot the local near field profiles of ω_1 and ω^θ in Figure 7. We observe that the "peak" of $-\omega_1$ locates at the z-axis where $r=0$, and is being pushed toward the origin as implied by the velocity field u^r, u^z. We denote by $(R_1(t), Z_1(t))$ the position at which $|\omega_1|$ achieves its maximum at time t. We have $R_1(t)=0$. At $(R_1(t), Z_1(t))$, the radial velocity u^r is zero, and the axial velocity u^z is negative, which pushes $(R_1(t), Z_1(t))$ toward the origin.

In Figure 8, we plot the local velocity field near the maximum of $-\omega^\theta$ and $-\omega_1$, respectively. We use the pseudocolor plots of $-\omega^\theta$ and $-\omega_1$ as the background, respectively, for the figure in the left and the right subplots, and mark the maximum of $-\omega^\theta$ or $-\omega_1$ with the red dot. The velocity field demonstrates a clear hyperbolic structure as depicted by Figure 4. And the velocity field clearly pushes the maximum $(R_1(t), Z_1(t))$ of $-\omega_1$ toward the origin.

In Figure 9, we show the local streamlines near the maximum of $-\omega^\theta$ in $\mathbb{R}^3$. The maximum of $-\omega^\theta$ locates on the red ring centered at $(0, Z_1(t))$ along the z-axis. In the left figure, we plot a set of streamlines that travel through the maximum ring from top to bottom. And in the right figure, we plot a set of streamlines that travel

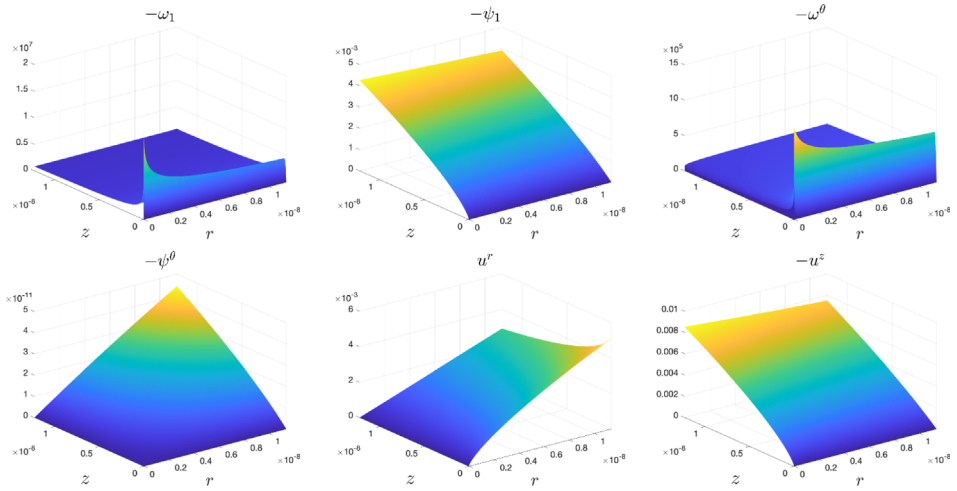

FIG. 6. *Profiles of* $-\omega_1$, $-\psi_1$, $-\omega^\theta$, $-\psi^\theta$, u^r, *and* $-u^z$ *near the origin at* $t = 1.6524635 \times 10^{-3}$.

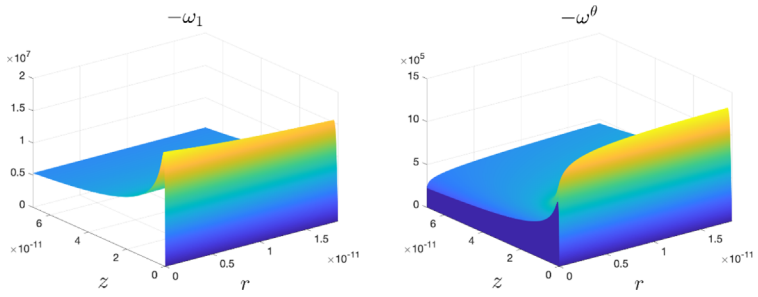

FIG. 7. *Further zoomed-in profiles of* $-\omega_1$ *and* $-\omega^\theta$ *near the origin at* $t = 1.6524635 \times 10^{-3}$.

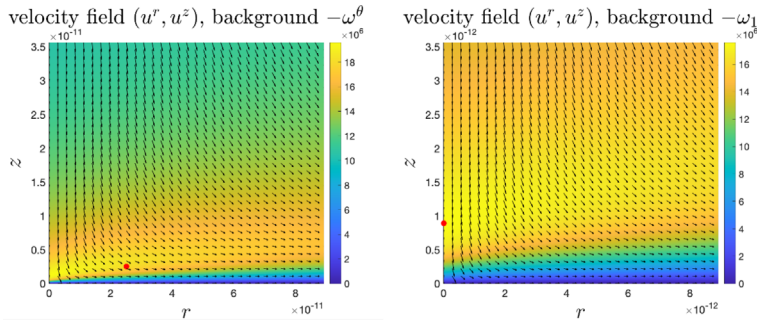

FIG. 8. *The local velocity field near the maximum of* $-\omega^\theta$ *and* $-\omega_1$. *The pseudocolor plot of* $-\omega^\theta$ *or* $-\omega_1$ *is the background, and the red dot is its maximum. (Figure in color online.)*

around the maximum ring from top to bottom. From Figure 9, we notice that the streamlines are axisymmetric, and do not form swirl around the z-axis.

In Figure 10, we show the curve of the maximum location of $-\omega_1$, Z_1, and the kinetic energy E, as functions of time. We can see that $Z_1(t)$ monotonically decreases to zero with t. The curve of $Z_1(t)$ seems to be convex, especially in time windows

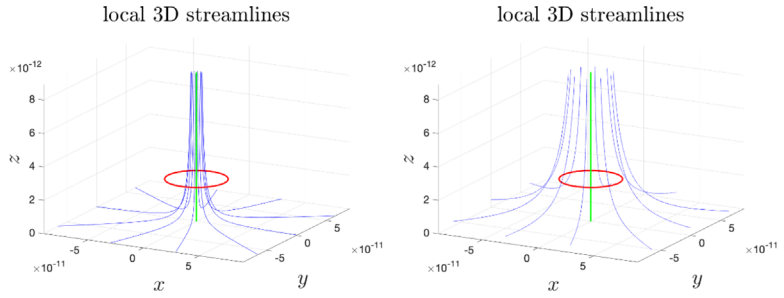

FIG. 9. *The local streamlines near the origin. The green pole is the z-axis, and the red ring is where* $-\omega^\theta$ *achieves its maximum. (Figure in color online.)*

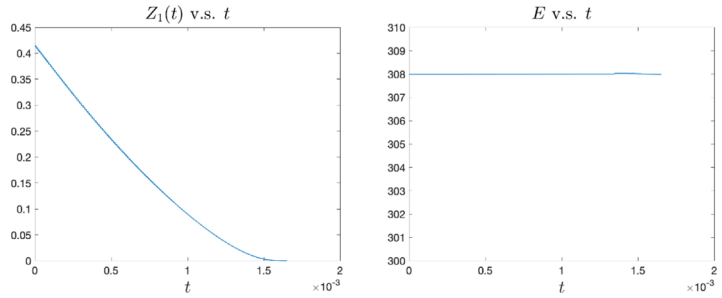

FIG. 10. *Curves of* Z_1 *and* E *as functions of time* t.

close to the stopping time. We refer to section 3.4 for more study of the behavior of $Z_1(t)$. The kinetic energy E, which is defined as

$$E = \frac{1}{2}\int_{\mathcal{D}} |u|^2 \,\mathrm{d}x = \pi \int_0^1 \int_0^{1/2} \left(|u^r|^2 + |u^z|^2\right) r \mathrm{d}r\mathrm{d}z,$$

for our axisymmetric case with no swirl, is a conservative quantity of the 3D Euler equations. In Figure 10, we can see that there is little change of the kinetic energy E as a function of time t. In fact, the major reason for the change of E in our computation is due to the update of adaptive mesh, where we need to interpolate ω_1 and ψ_1 from an old mesh to a new mesh. Since the new adaptive mesh will focus more on the near field around the origin, the far field velocity field might lose some accuracy, leading to a change in the kinetic energy E. However, such an update of adaptive mesh occurs only 35 times out of the total 65000 iterations in time, and the change in the kinetic energy E in each update is negligible. By the end of the computation, the change in the kinetic energy E is at most 1.4×10^{-4} of the magnitude of E.

3.2. Evidence for a potential self-similar blow-up. We observe a potential self-similar blow-up in our numerical solution. To check the self-similar property, we visualize the local profile of the rescaled ω_1 near the origin. Recall that $(0, Z_1)$ is the maximum location of $-\omega_1$, we define

$$\hat{\omega}_1(\hat{r}, \hat{z}, t) = \omega_1\left(Z_1(t)\hat{r}, Z_1(t)\hat{z}, t\right) / \|\omega_1(t)\|_{L^\infty},$$

as the rescaled version of ω_1. The above definition rescales the magnitude of $|\hat{\omega}_1|$ to 1, and rescales the maximum location of $|\hat{\omega}_1|$ to $(\hat{r}, \hat{z}) = (0, 1)$. We plot the profiles of $-\hat{\omega}_1$ near the origin at different time instants and the contours of $-\hat{\omega}_1(\hat{r}, \hat{z})$ at

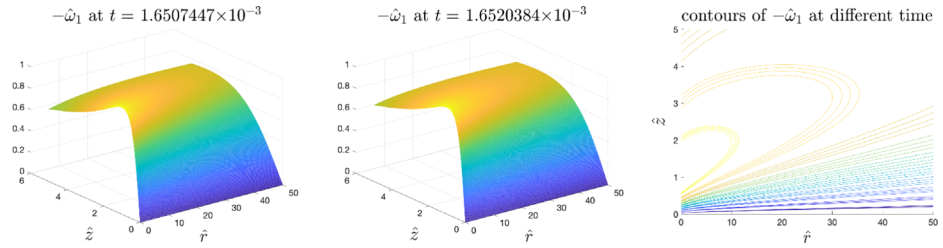

FIG. 11. *Left and middle: Local profiles of* $-\hat{\omega}_1$ *at* $t = \{1.6507447, 1.6520384\} \times 10^{-3}$. *Right: Local contours of* $-\hat{\omega}_1$ *at* $t = \{1.6507447, 1.6512953, 1.6517173, 1.6520384\} \times 10^{-3}$.

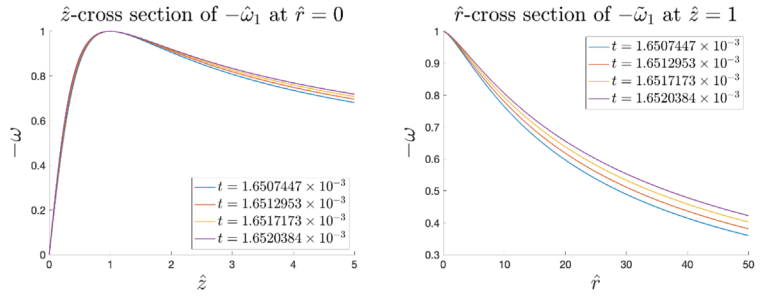

FIG. 12. *Cross sections of* $-\hat{\omega}_1$ *at different times.*

different times in Figure 11. The profile of $-\hat{\omega}_1$ seems to change slowly in the late time, indicating a potential self-similar structure of the blow-up profile near the origin. In other words, $x_0 = 0$ in the self-similar ansatz (2.6).

In Figure 12, we plot the cross sections of $-\hat{\omega}_1$ at $\hat{r} = 0$ and $\hat{z} = 1$. The cross section at $\hat{r} = 0$ shows a good potential for a self-similar blow-up, while the cross section at $\hat{z} = 1$ shows that the blow-up profile has not converged to a self-similar profile yet. This is reasonable because although we are very close to the potential blow-up time, the strong collapsing along the z-direction and the effect of round-off errors prevent us from continuing the computation. We refer to section 4 where we use the dynamic rescaling method and indeed observe numerically the convergence to the potential self-similar profile.

3.3. Resolution study. We perform resolution study on the numerical solutions of (1.5) to confirm the accuracy of our numerical solutions. We first simulate the equations on spatial resolutions of $256k \times 256k$ with $k = 1, 2, \ldots, 6$. The highest resolution we used is 1536×1536. Next, for the numerical solution at resolution $256k \times 256k$, we compute its sup-norm relative error in several chosen quantities at selected time instants using the numerical solution at resolution $256(k+1) \times 256(k+1)$ as the reference, for $k = 1, 2, \ldots, 5$. Finally, we use the relative error obtained above to estimate the convergence order of the numerical method.

We consider two types of quantities. The first type is the function of the solutions. Here we consider the magnitude of ω_1, $\|\omega_1\|_{L^\infty}$, the maximum norm of vorticity, $\|\omega\|_{L^\infty}$, and the kinetic energy E. We remark that $\|\omega_1\|_{L^\infty}$ and $\|\omega\|_{L^\infty}$ only depend on the local field near the origin, and E should be considered as a global quantity. The second type is the vector fields of ω_1, ψ_1, u^r, and u^z that are actively participating in the simulated system (1.5).

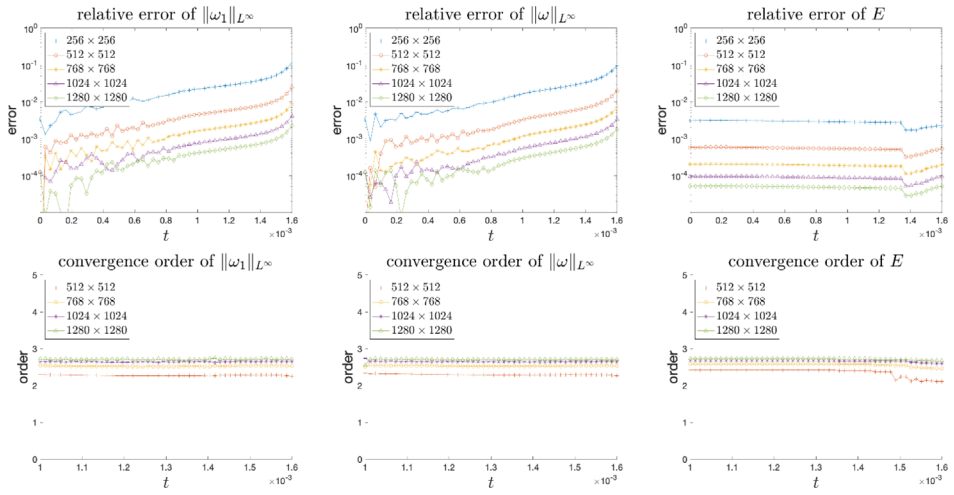

FIG. 13. *Relative errors and convergence orders of* $\|\omega_1\|_{L^\infty}$, $\|\omega\|_{L^\infty}$, *and* E *in sup-norm.*

For each quantity, we use q_k to represent the estimate we get at resolution $256k \times 256k$. Then the sup-norm relative error e_k is defined as

$$e_k = \|q_k - q_{k+1}\|_{L^\infty} / \|q_{k+1}\|_{L^\infty}.$$

If q_k is a vector field, we first interpolate it to the reference resolution $256(k+1) \times 256(k+1)$, and then compute the relative error as above. The convergence order of the error β_k at this resolution can be estimated via

$$\beta_k = \log\left(\frac{e_{k-1}}{e_k}\right) \Big/ \log\left(\frac{k}{k-1}\right).$$

In Figure 13, we plot the relative error of the quantities $\|\omega_1\|_{L^\infty}$, $\|\omega\|_{L^\infty}$, and E for $t \in [0, 1.6 \times 10^{-3}]$, and the convergence order of the error in the late time $t \in [1\times10^{-3}, 1.6\times10^{-3}]$. We observe a numerical convergence with order slightly higher than 2. The convergence order is quite stable in the time interval of our computation.

In Table 1, we list the relative error and convergence order of the vector fields at $t = 1.6 \times 10^{-3}$. The convergence order stays well above 2, suggesting at least a second-order convergence for our numerical solver of the 3D axisymmetric Euler equations.

3.4. Scaling analysis. In this section, we quantify the scaling property of the potential blow-up observed in our computation. This scaling analysis will give more supporting evidence that the potential blow-up satisfies the BKM blow-up criterion. It also uncovers more properties of the potential blow-up.

As discussed in (2.6) of section 2.3, if there is a self-similar blow-up, the scaling invariant property of the 3D Euler equations will ensure that $\|\omega\|_{L^\infty} \sim 1/(T-t)$ and $\|\psi_{1,z}\|_{L^\infty} \sim 1/(T-t)$. Therefore, we examine this property by regressing $\|\omega\|_{L^\infty}^{-1}$ and $\|\psi_{1,z}\|_{L^\infty}^{-1}$ against t, respectively. More specifically, for a quantity v, which is either $\|\omega\|_{L^\infty}^{-1}$ or $\|\psi_{1,z}\|_{L^\infty}^{-1}$, we perform the least square fitting of the model

$$v \sim a \cdot (b - t),$$

in searching for constants a and b, where a is the negated slope of the fitted line, and b can be considered as the estimate time of the blow-up. In Figure 14, we visualize

TABLE 1
Relative errors and convergence orders of ω_1, ψ_1, u^r and u^z in sup-norm.

	Sup-norm relative error at $t = 1.6 \times 10^{-3}$			
Mesh size	ω_1	Order	ψ_1	Order
256×256	2.545×10^{-1}	-	5.912×10^{-3}	-
512×512	5.478×10^{-2}	2.216	1.168×10^{-3}	2.340
768×768	1.969×10^{-2}	2.524	4.136×10^{-4}	2.560
1024×1024	9.189×10^{-3}	2.655	1.926×10^{-4}	2.656
1280×1280	5.008×10^{-3}	2.720	1.050×10^{-4}	2.719
	Sup-norm relative error at $t = 1.6 \times 10^{-3}$			
Mesh size	u^r	Order	u^z	Order
256×256	2.035×10^{-2}	-	8.095×10^{-3}	-
512×512	3.954×10^{-3}	2.364	1.533×10^{-3}	2.310
768×768	1.405×10^{-3}	2.552	5.793×10^{-4}	2.556
1024×1024	6.540×10^{-4}	2.658	2.699×10^{-4}	2.655
1280×1280	3.594×10^{-4}	2.682	1.472×10^{-4}	2.719

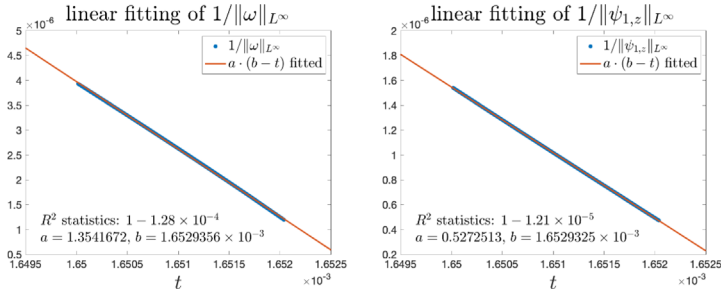

FIG. 14. *Linear fitting of $1/\|\omega\|_{L^\infty}$ and $1/\|\psi_{1,z}\|_{L^\infty}$ with time.*

the data points and the fitted line using data between $t = 1.6500174 \times 10^{-3}$ and $t = 1.6520384 \times 10^{-3}$. The R^2 of the fitting between $\|\omega\|_{L^\infty}^{-1}$ and t is $1 - 1.28 \times 10^{-4}$, and the R^2 of the fitting between $\|\psi_{1,z}\|_{L^\infty}^{-1}$ and t is $1 - 1.21 \times 10^{-5}$. Such high R^2 values show strong linear relation between $\|\omega\|_{L^\infty}^{-1}$, $\|\psi_{1,z}\|_{L^\infty}^{-1}$, and t. Moreover, the fittings of the two quantities estimate the blow-up time to be $b = 1.6529356 \times 10^{-3}$ and $b = 1.6529325 \times 10^{-3}$, respectively. These two blow-up times agree with each other up to six digits. Therefore, Figure 14 provides further evidence that the 3D Euler equations develop a potential finite-time singularity.

We next move to fit the scaling factors c_l and c_ω used in the self-similar ansatz (2.6) of the solutions. Since the functions Ω and Ψ are time-independent in (2.6), we should have that

$$Z_1 \sim (T-t)^{c_l}, \quad \|\omega_1\|_{L^\infty}^{-1} \sim (T-t)^{c_\omega},$$

where we recall that $Z_1 = Z_1(t)$ is the z-coordinate of the maximum location of $-\omega_1$. Due to the unknown powers c_l and c_ω, the direct fitting of the above model is nonlinear. Therefore, we turn to a searching algorithm for the power variable. Specifically, for a quantity v, that is either Z_1 or $\|\omega_1\|_{L^\infty}^{-1}$, we search for a power c such that the linear regression of

$$v^{1/c} \sim a \cdot (b-t)$$

has the largest R^2 value up to some error tolerance. We will start with a guessed window of the power c, and then exhaust the value of c within the window up to some error tolerance, and choose c with the largest R^2 value. If the optimal c we searched for falls on the boundary of the current window, we then adaptively adjust the window size and location, and repeat the above procedure. When the optimal searched c falls within the interior of the window, we stop the searching.

In Figure 15, we demonstrate the result of the searching. We can see that with the chosen c, the linear regression achieves a very high R^2 value, suggesting a strong linear relation. The relative error between the estimated blow-up time and the previous estimate smaller than 7.8×10^{-5}. Moreover, the searching suggests that $c_l \approx 4.20$ and $c_\omega \approx 1.41$, and these estimated values of c_l and c_ω satisfy the scaling relation $c_\omega = 1 + \alpha c_l$ in (2.8) approximately.

It is worth emphasizing that the estimated c_l is well above 1, and this explains the convex curve of $Z_1(t)$ as observed in Figure 10 in section 3.1.

We remark that we did not perform the searching algorithm with $\|\psi_1\|_{L^\infty}$ to find out the scaling factor c_ψ, so that we could check the other scaling relation $c_\psi = 1 - c_l$ in (2.8). This is because $\|\psi_1\|_{L^\infty}$ is mainly affected by the far field behavior of ψ_1, as shown in Figure 6. However, the self-similar ansatz (2.6) is only valid in the near field, so such fitting is meaningless. In fact, the good fitting between $\|\psi_{1,z}\|_{L^\infty}^{-1}$ and t already implies that $c_\psi = 1 - c_l$, because the self-similar ansatz suggests that $\|\psi_{1,z}\|_{L^\infty}^{-1} \sim (T-t)^{c_\psi + c_l}$.

Finally, we perform the above fitting of different quantities using different spatial resolutions, and summarize the results in Table 2. We can see that the fitting has excellent quality at all spatial resolutions, and the fitted parameters are consistent across different spatial resolutions.

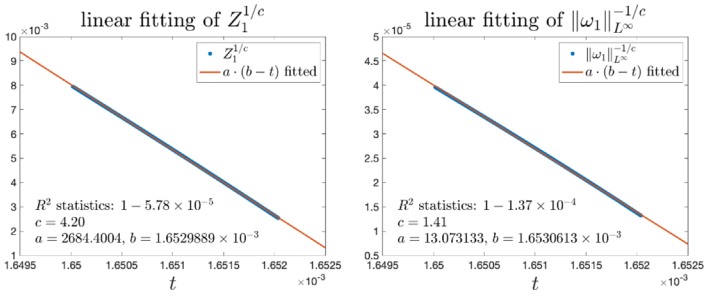

FIG. 15. *Linear fitting of* $Z_1^{1/c}$ *and* $\|\omega_1\|_{L^\infty}^{-1/c}$ *with time.*

TABLE 2
Fitting results of $\|\omega\|_{L^\infty}^{-1}$, $\|\psi_{1,z}\|_{L^\infty}^{-1}$, Z_1, *and* $\|\omega_1\|_{L^\infty}^{-1}$ *at different mesh sizes.*

Mesh size	$1/\|\omega\|_{L^\infty}$		$1/\|\psi_{1,z}\|_{L^\infty}$	
	$10^3 \times b$	R^2	$10^3 \times b$	R^2
1024×1024	1.6529356	0.99987	1.6529325	0.99999
1280×1280	1.6527953	1.00000	1.6528189	1.00000
1536×1536	1.6525824	1.00000	1.6527396	1.00000

Mesh size	Z_1			$1/\|\omega_1\|_{L^\infty}$		
	c	$10^3 \times b$	R^2	c	$10^3 \times b$	R^2
1024×1024	4.20	1.6529889	0.99994	1.41	1.6530613	0.99986
1280×1280	4.21	1.6527877	0.99999	1.42	1.6527894	1.00000
1536×1536	4.25	1.6526864	1.00000	1.41	1.6526953	1.00000

4. The dynamic rescaling formulation. In order to better study the potential self-similar singularity as we have observed in section 3.2, we add extra scaling terms to (1.5) and write

$$\tilde{\omega}_{1,\tau} + \left(\tilde{c}_l\xi + \tilde{u}^{\xi}\right)\tilde{\omega}_{1,\xi} + \left(\tilde{c}_l\zeta + \tilde{u}^{\zeta}\right)\tilde{\omega}_{1,\zeta} = \left(c_\omega - (1-\alpha)\tilde{\psi}_{1,\zeta}\right)\tilde{\omega}_1, \tag{4.1a}$$

$$-\tilde{\psi}_{1,\xi\xi} - \tilde{\psi}_{1,\zeta\zeta} - \frac{3}{\xi}\tilde{\psi}_{1,\xi} = \tilde{\omega}_1\xi^{\alpha-1}, \tag{4.1b}$$

$$\tilde{u}^{\xi} = -\xi\tilde{\psi}_{1,\zeta}, \quad \tilde{u}^{\zeta} = 2\tilde{\psi}_1 + \xi\tilde{\psi}_{1,\xi}, \tag{4.1c}$$

where $\tilde{c}_l = \tilde{c}_l(\tau)$, $\tilde{c}_\omega = \tilde{c}_\omega(\tau)$ are scalar functions of τ. In (4.1a), the terms $\tilde{c}_l\xi\partial_\xi$ and $\tilde{c}_l\zeta\partial_\zeta$ stretch the solutions in space to maintain a finite support of the self-similar blow-up solution. The term $\tilde{c}_\omega\tilde{\omega}_1$ acts as a damping term to ensure that the magnitude of $\tilde{\omega}_1$ remains finite. The combined effect of these terms dynamically rescales the solution to capture the potential self-similar profile. Such dynamic rescaling strategy has widely been used in the study of singularity formation of nonlinear Schrödinger equations as in [45, 35, 36, 34, 47]. And recently it has been used to study singularity formation of the 3D Euler equations as in [27, 6, 9].

If we define

$$\tilde{c}_\psi(\tau) = \tilde{c}_\omega(\tau) + (1+\alpha)\tilde{c}_l(\tau), \tag{4.2}$$

we can check that (4.1) admits the following solution:

$$\begin{aligned}\tilde{\omega}_1(\xi,\zeta,\tau) &= \tilde{C}_\omega(\tau)\omega_1\left(\tilde{C}_l(\tau)\xi, \tilde{C}_l(\tau)\zeta, t(\tau)\right),\\ \tilde{\psi}_1(\xi,\zeta,\tau) &= \tilde{C}_\psi(\tau)\psi_1\left(\tilde{C}_l(\tau)\xi, \tilde{C}_l(\tau)\zeta, t(\tau)\right),\end{aligned} \tag{4.3}$$

where (ω_1, ψ_1) is the solution to (1.5), and

$$\begin{aligned}&\tilde{C}_\omega(\tau) = \exp\left(\int_0^\tau \tilde{c}_\omega(s)\mathrm{d}s\right), \quad \tilde{C}_\psi(\tau) = \exp\left(\int_0^\tau \tilde{c}_\psi(s)\mathrm{d}s\right),\\ &\tilde{C}_l(\tau) = \exp\left(-\int_0^\tau \tilde{c}_l(s)\mathrm{d}s\right), \quad t'(\tau) = \tilde{C}_\psi(\tau)\tilde{C}_l(\tau) = \tilde{C}_\omega(\tau)\tilde{C}_l^{-\alpha}(\tau).\end{aligned}$$

The new equations (4.1) leave us with two degrees of freedom: we are free to choose $\{\tilde{c}_l(\tau), \tilde{c}_\omega(\tau)\}$. This allows us to impose the following normalization conditions:

$$\tilde{\omega}_1(0,1,\tau) = -1, \quad \tilde{\omega}_{1,\zeta}(0,1,\tau) = 0, \quad \text{for } \tau \geq 0. \tag{4.4}$$

These two conditions will help fix the maximum value of $-\tilde{\omega}_1$ at 1 and the maximum location at $(\xi,\zeta) = (0,1)$.

One way to enforce the normalization conditions, as used in many literatures like [27, 40], is to first enforce them at $\tau = 0$ using the scaling invariant relation (2.7), and then enforce their time derivatives to be zero

$$\frac{\partial}{\partial\tau}\tilde{\omega}_1(0,1,\tau) = 0, \quad \frac{\partial}{\partial\tau}\tilde{\omega}_{1,\zeta}(0,1,\tau) = 0, \quad \text{for } \tau \geq 0. \tag{4.5}$$

Using (4.1a), the above conditions are equivalent to

$$\begin{aligned}\tilde{c}_l(\tau) =& -2\tilde{\psi}_1(0,1,\tau) - (1-\alpha)\tilde{\psi}_{1,\zeta\zeta}(0,1,\tau)\frac{\tilde{\omega}_1(0,1,\tau)}{\tilde{\omega}_{1,\zeta\zeta}(0,1,\tau)},\\ \tilde{c}_\omega(\tau) =& (1-\alpha)\tilde{\psi}_{1,\zeta}(0,1,\tau).\end{aligned} \tag{4.6}$$

However, it is hard to evaluate (4.6) accurately, because it requires calculating second-order derivatives. More importantly, due to the complicated nonlinear nature of (4.1a), even if (4.6) can be accurately evaluated, the temporal discretization (Runge–Kutta method) makes it difficult to enforce (4.4) exactly for the next time step. As a result, imposing (4.5) is not as helpful to preserve the normalization conditions (4.4) in the following time steps. The maximum magnitude and location will gradually change in time, which makes it difficult to compute the self-similar profile numerically.

4.1. The operator splitting strategy. To enforce the normalization conditions (4.4) accurately at every time step, we utilize the operator splitting method and rewrite (4.1a) as

$$\tilde{\omega}_{1,\tau} = F(\tilde{\omega}_1) + G(\tilde{\omega}_1), \tag{4.7}$$

where $F(\tilde{\omega}_1) = -\tilde{u}^{\xi}\tilde{\omega}_{1,\xi} - \tilde{u}^{\zeta}\tilde{\omega}_{1,\zeta} - (1-\alpha)\tilde{\psi}_{1,\zeta}\tilde{\omega}_1$ contains the original terms in (1.5a), and $G(\tilde{\omega}_1) = -\tilde{c}_l\xi\tilde{\omega}_{1,\xi} - \tilde{c}_l\zeta\tilde{\omega}_{1,\zeta} + \tilde{c}_\omega\tilde{\omega}_1$ is the linear part that controls the rescaling. Here we view $\tilde{\psi}_1$ as a function of $\tilde{\omega}_1$ through the Poisson equation (4.1b). The operator splitting method allows us to solve (4.1a) by solving $\tilde{\omega}_{1,\tau} = F(\tilde{\omega}_1)$ and $\tilde{\omega}_{1,\tau} = G(\tilde{\omega}_1)$ alternatively.

We can use the standard Runge–Kutta method to solve $\tilde{\omega}_{1,\tau} = F(\tilde{\omega}_1)$. As for $\tilde{\omega}_{1,\tau} = G(\tilde{\omega}_1)$, we notice that there is a closed form solution for the initial value problem

$$\tilde{\omega}_1(\xi,\zeta,\tau) = \tilde{C}_\omega(\tau)\tilde{\omega}_1\left(\tilde{C}_l(\tau)\xi, \tilde{C}_l(\tau)\zeta, 0\right), \tag{4.8}$$

where $\tilde{C}_\omega(\tau) = \exp\left(\int_0^\tau \tilde{c}_\omega(s)\mathrm{d}s\right)$ and $\tilde{C}_l(\tau) = \exp\left(-\int_0^\tau \tilde{c}_l(s)\mathrm{d}s\right)$.

In the first step, solving $\tilde{\omega}_{1,\tau} = F(\tilde{\omega}_1)$ will violate the normalization conditions (4.4). But we will correct this error in the second step by solving $\tilde{\omega}_{1,\tau} = G(\tilde{\omega}_1)$ with a smart choice of $\tilde{C}_l$ and $\tilde{C}_\omega$ in (4.8). In other words, at every time step when we solve $\tilde{\omega}_{1,\tau} = G(\tilde{\omega}_1)$, we can exactly enforce (4.4) by properly choosing $\tilde{C}_l$ and $\tilde{C}_\omega$ in (4.8). We could also adopt Strang's splitting [53] for better temporal accuracy.

4.2. Numerical settings. Now we numerically solve the dynamic rescaling formulation (4.1). For the initial condition, we use the solution obtained from the final iteration of the adaptive mesh method in section 3.1, and use the relation (2.7) to enforce the normalization conditions (4.5). Now that the maximum location of $\tilde{\omega}_1$ is pinned at $(\xi,\zeta) = (0,1)$, we focus on a large computational domain

$$\mathcal{D}' = \{(\xi,\zeta) : 0 \le \xi \le D, 0 \le \zeta \le D/2\},$$

with domain size $D = 1\times 10^5$. The reason for such large domain size is because under the normalization of the dynamic rescaling formulation, the original computational domain $(r,z) \in [0,1]\times[0,1/2]$ is now equivalent to $(\xi,\zeta) \in [0,1/Z_1]\times[0,1/2/Z_1]$. This domain grows large quickly as Z_1 tends to zero. While we adopt the boundary conditions at $\xi = 0$ and $\zeta = 0$ of (1.5) in section 2.1, we need to find a good far field boundary conditions for $\tilde{\psi}_1$. Due to extra stretching terms, the far field boundary for $\tilde{\psi}_1$ will no longer correspond to the far field boundary for ψ_1, namely $r = 1$ and $z = 1/2$. However, we notice that $\psi_{1,r}$ decays rapidly with respect to r, and $\psi_{1,z}$ decays rapidly with respect to z. For example, Figure 16 shows the decay of $\psi_{1,r}$ as $r \to 1$ and the decay of $\psi_{1,z}$ as $z \to 1/2$ for the solution to (1.5) at $t = 1.6524635\times 10^{-3}$. Therefore, it is reasonable to impose the zero Neumann boundary condition at the far field boundaries of $\mathcal{D}'$: $\xi = D$ and $\zeta = D/2$. Due to the size of the computation domain $\mathcal{D}'$ and the presence of the vortex stretching terms, the error introduced by this

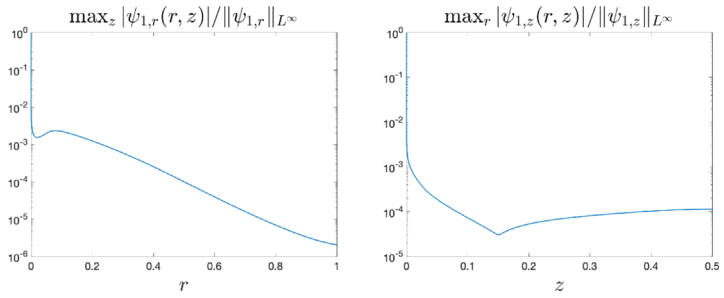

FIG. 16. *Decay of the derivatives of* ψ_1.

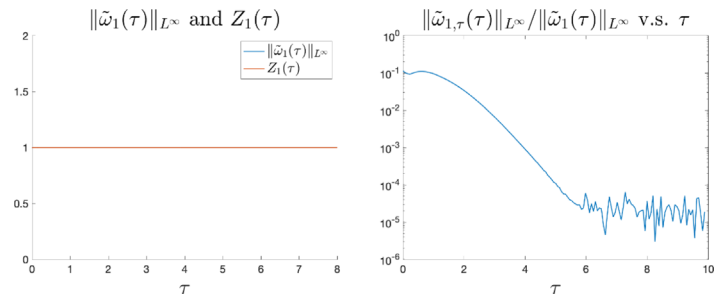

FIG. 17. *Left: Curves of the normalized quantities* $\|\tilde{\omega}_1(\tau)\|_{L^\infty}$ *and* $Z_1(\tau)$. *Right: Curve of the relative time derivative strength* $\|\tilde{\omega}_{1,\tau}(\tau)\|_{L^\infty}/\|\tilde{\omega}_1(\tau)\|_{L^\infty}$.

boundary condition will have little influence on the near field around $(\xi,\zeta)=(0,1)$. We will discuss in detail the influence of the domain size D in section 4.4 and in the end of section 5.1.

We remark that we still need the adaptive mesh in the r- and z-directions, because we not only need to cover a very large field, but also need to focus around $(\xi,\zeta)=(0,1)$. The adaptive mesh that we use to solve the dynamic rescaling formulation will not change during the computation, since the dynamically rescaled vorticity has its maximum location fixed at $(\xi,\zeta)=(0,1)$ for all times instead of traveling toward the origin.

4.3. Convergence to the steady state. We solve (4.1) until it converges to a steady state. In the left subplot of Figure 17, we monitor how the normalization conditions (4.5) are enforced. The two normalized quantities, $\|\tilde{\omega}_1(\tau)\|_{L^\infty}$ and $Z_1(\tau)$, are essentially fixed at 1, and in fact, they deviate from 1 by less than 5.14×10^{-4}. In the right subplot of Figure 17, We view the system (4.1) as an ODE of $\tilde{\omega}_1$ as in (4.7), and plot the relative strength of the time derivative

$$\|\tilde{\omega}_{1,\tau}\|_{L^\infty}/\|\tilde{\omega}_1\|_{L^\infty}=\|F(\tilde{\omega}_1)+G(\tilde{\omega}_1)\|_{L^\infty}/\|\tilde{\omega}_1\|_{L^\infty},$$

as a function of time τ. This relative strength of the time derivative has a decreasing trend and drops below 8.18×10^{-6} near the end of the computation, which implies that we are very close to the steady state.

When the solution of (4.1) converges to a steady state, $\tilde{\omega}_1$ and $\tilde{\psi}_1$ are independent of the time τ. Therefore, we should have the following relation from (4.3):

$$\omega_1(r,z,t)\sim\tilde{C}_\omega^{-1}(\tau(t))\tilde{\omega}_1\left(\tilde{C}_l^{-1}(\tau(t))r,\tilde{C}_l^{-1}(\tau(t))z\right),$$
$$\psi_1(r,z,t)\sim\tilde{C}_\psi^{-1}(\tau(t))\tilde{\psi}_1\left(\tilde{C}_l^{-1}(\tau(t))r,\tilde{C}_l^{-1}(\tau(t))z\right),$$

where $\tau = \tau(t)$ is the rescaled time variable. Comparing the above relation with the ansatz stated in (2.6), we conclude that

$$c_l = -\frac{\tilde{c}_l}{\tilde{c}_\omega + \alpha \tilde{c}_l}, \quad c_\omega = \frac{\tilde{c}_\omega}{\tilde{c}_\omega + \alpha \tilde{c}_l}, \quad c_\psi = \frac{\tilde{c}_\psi}{\tilde{c}_\omega + \alpha \tilde{c}_l}. \tag{4.9}$$

We remark that assuming (4.2), the above relation naturally guarantees that the scaling relation (2.8) holds true.

In Figure 18, we show the curves of scaling factors $\tilde{c}_l$, $\tilde{c}_\omega$ for the dynamic rescaling formulation (4.1) and c_l, c_ω for the self-similar ansatz (2.6). We observe a relatively fast convergence to the steady state as time increases. The converged values $c_l = 4.549$ and $c_\omega = 1.455$ are close to the approximate values obtained in section 3.4. Moreover, they also satisfy the relation (2.8).

The approximate steady states of $\tilde{\omega}_1$ and $\tilde{\psi}_1$ are plotted in Figure 19. We see that both $\tilde{\omega}_1$ and $\tilde{\psi}_1$ are relatively flat in ξ, suggesting a possible 1D structure of their profiles. While both functions have weak dependence on ξ, $-\tilde{\omega}_1$ seems to tilt up

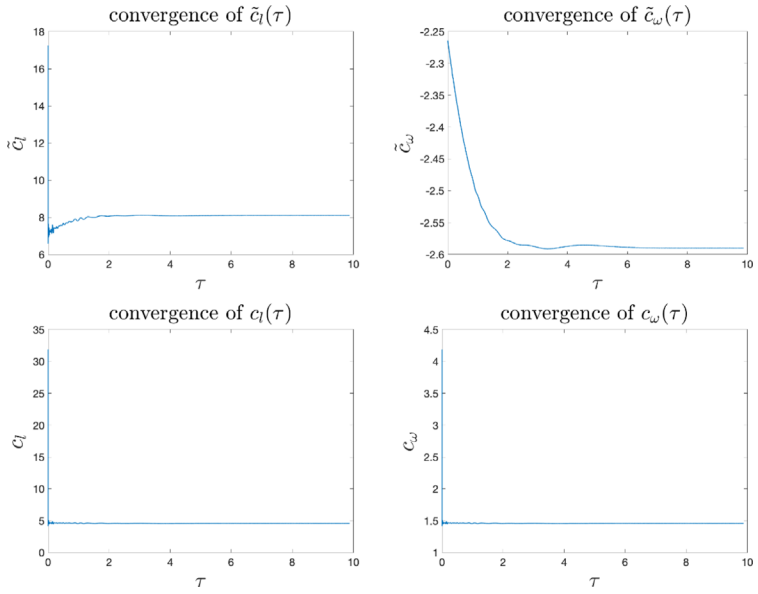

FIG. 18. *Convergence curves of the scaling factors using dynamic rescaling method. Top row:* $\tilde{c}_l$ *and* $\tilde{c}_\omega$*. Bottom row:* c_l *and* c_ω*.*

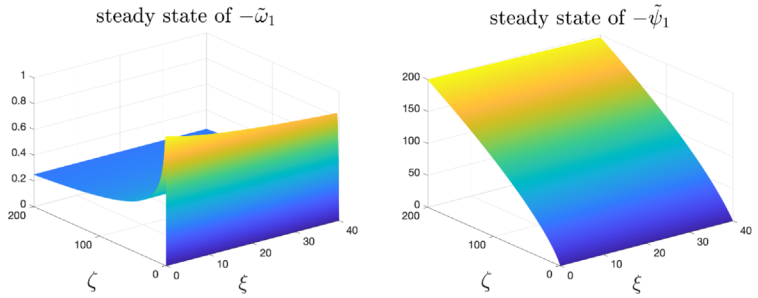

FIG. 19. *Steady states of* $-\tilde{\omega}_1$ *and* $-\tilde{\psi}_1$*.*

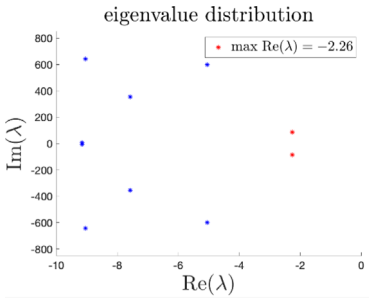

FIG. 20. *Top* 10 *eigenvalues of the Jacobian with the largest real part.*

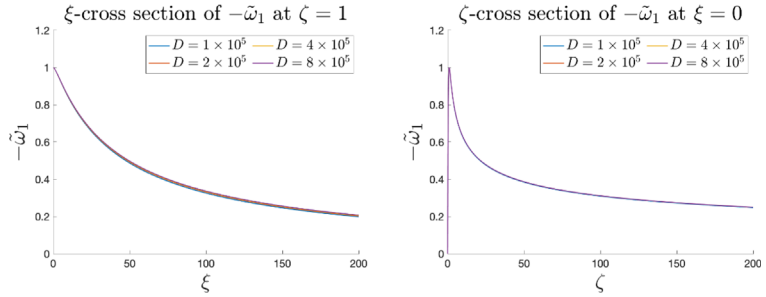

FIG. 21. *Cross sections of steady states of* $-\tilde{\omega}_1$ *with different domain size* D.

around $\xi = 0$ a little bit. The shape of the steady states looks similar to the shape of the profiles we obtained via the adaptive mesh at the stopping time in Figure 7.

To study the stability of the steady states, we linearize the time-evolution equation (4.1) of $\tilde{\omega}_1$ near the steady states, and compute the eigenvalues of the Jacobian matrix. The top few eigenvalues with largest real part are plotted in Figure 20. We see that the eigenvalues have negative real part, which demonstrates the stability of our potential self-similar finite-time blow-up.

4.4. The domain size study. Ideally, the dynamic rescaling formulation (4.1) should be solved in the first quadrant $\mathcal{D}'_\infty = \{(\xi, \zeta) : \xi \geq 0, \zeta \geq 0\}$. In section 2, we use a large rectangular region $\mathcal{D}' = [0, D] \times [0, D/2]$, with domain size $D = 10^5$, to approximate the unbounded domain $\mathcal{D}'_\infty$ and propose using the Neumann boundary condition at the far field.

We study how the domain size would influence our steady state solution by extending the domain size and considering $D = 1 \times 10^5, 2 \times 10^5, 4 \times 10^5, 8 \times 10^5$. Using these four different domain sizes, we solve the dynamic rescaling formulation (4.1) to its steady state. Figure 21 is the cross section comparison of the steady state of $\tilde{\omega}_1$. We also list the scaling factor c_l with different domain size D in Table 3. We can see that, with significant larger domain size, the steady state is nearly the same, and the scaling factor is almost the same. This shows our choice of domain size $D = 10^5$ is large enough to approximate the steady state well.

5. The Hölder exponent and the dimension in the potential blow-up. Starting this section, we will no longer fix the Hölder exponent $\alpha = 0.1$.

5.1. The Hölder exponent α. In his study of the finite-time blow-up of the axisymmetric Euler equations with no swirl and with Hölder continuous initial data

TABLE 3
The scaling factor c_l with different domain size D.

D	1×10^5	2×10^5	4×10^5	8×10^5
c_l	4.549	4.546	4.545	4.545

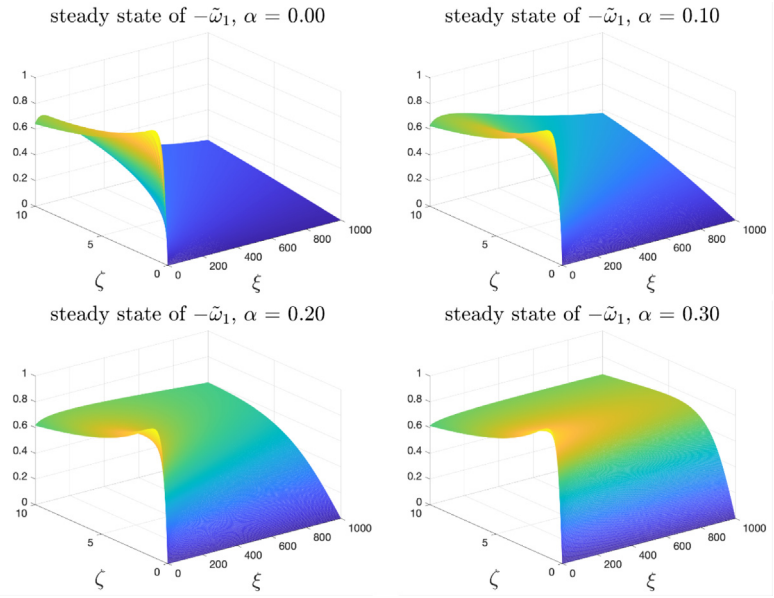

FIG. 22. *Steady states of $-\tilde{\omega}_1$ with different α in $\mathbb{R}^3$.*

[20], Elgindi assumes that α is very close to zero, smaller than 10^{-14}. Such small value of α is used to control the higher order terms of α in Elgindi's proof. However, as stated in Conjecture 8 of [18] by Drivas and Elgindi, such a blow-up may still hold for a range of $\alpha \in (0, 1/3)$ for the 3D Euler equations. For $\alpha > 1/3$, it has been shown by [54, 50, 51, 49, 16, 1] that the solution will be globally regular.

Therefore, we try different Hölder exponent α and explore the window of α that admits potential finite-time blow-up. For each α, we first use the adaptive mesh method to solve (1.5) close enough to its potential blow-up time, and then use the dynamic rescaling method (4.1) to continue the computation and capture the self-similar profile.

For our 3D axisymmetric Euler equations with initial data (2.5) with $\alpha = 0.0$, 0.1, 0.2, 0.3, we obtain strong evidence for the formation of self-similar singularity. The steady states of the solutions are plotted in Figure 22. We can see that as α increases, $\tilde{\omega}_1$ will have weaker dependence on ξ, and the self-similar profile becomes more and more one-dimensional. We plot the cross sections of the steady states of $\tilde{\omega}_1$ in Figure 23. As α increases, $-\tilde{\omega}_1(\xi, 1)$ becomes more and more flat, especially in the local window around $\xi = 0$. Moreover, $-\tilde{\omega}_1(0, \zeta)$ seems to be insensitive to the value of α. The cross sections of the stead states of $\tilde{\psi}_1$ in Figure 24 shows that as α increases, $-\tilde{\psi}_1(0, \zeta)$ becomes more and more like a linear function.

As α increases, c_l increases rapidly. We can see from Table 4 that c_l is more than 100 when $\alpha = 0.3$. Such large c_l can cause a lot of trouble for our adaptive mesh method, as the collapsing speed of the solution is extremely fast. Fortunately,

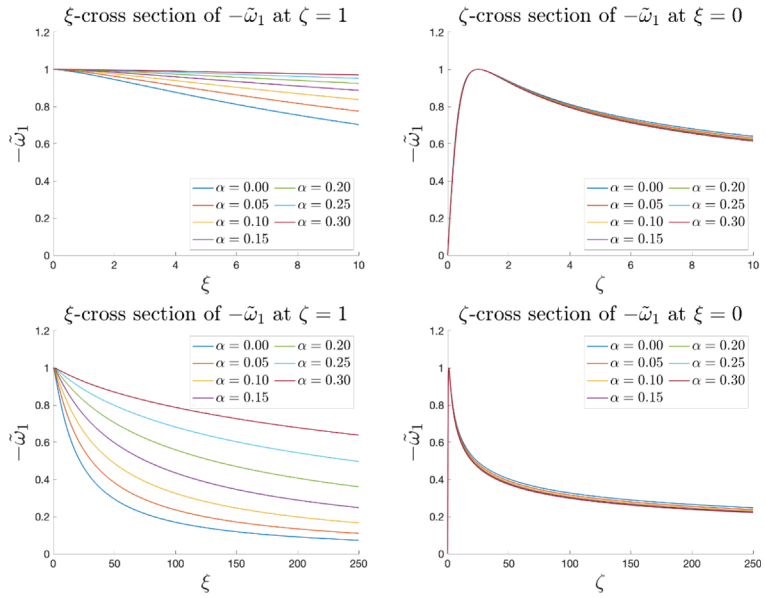

FIG. 23. *Cross sections of steady states of* $-\tilde{\omega}_1$ *with different* α. *Top row: On a local window. Bottom row: On a larger window.*

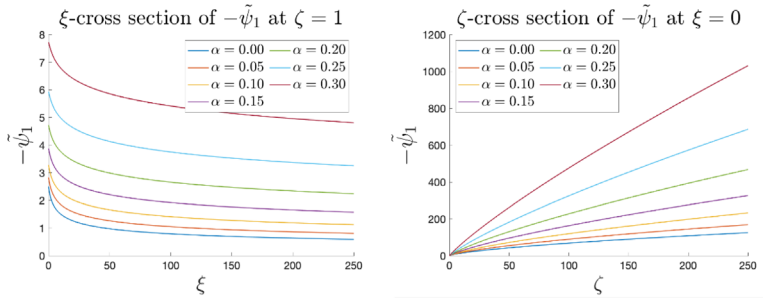

FIG. 24. *Cross sections of steady states of* $-\tilde{\psi}_1$ *with different* α.

TABLE 4
The scaling factor c_l *with different* α *in the* 3*D case.*

α	0.00	0.05	0.10	0.15	0.20	0.25	0.30
c_l	3.248	3.771	4.549	5.818	8.270	15.00	112.8

the dynamic rescaling method is stable with large c_l, as the extra stretching term can control the rate of collapse. Based on observation of the rapid increase of c_l as α approaches α^*, we conjecture that c_l will tend to infinity as α tends to α^*. It is interesting to notice that when $\alpha = 0.0$, the scaling factor c_l is approximately 3.248, which doesn't seem special nor implies any degeneracy. In fact, when $\alpha = 0$, our initial data (2.5) of ω_1 is smooth in the axisymmetric variable (r, z), but when we lift it to $\mathbb{R}^3$, the vorticity $\omega = \omega^\theta e_\theta$ will have singularity due to the coordinate singularity of e_θ. In this case, the symmetry axis can be viewed as a boundary in the (r, z)-plane.

For $\alpha > 0.30$, like $\alpha = 0.31, 0.40, 0.50$, we observe that although $\|\tilde{\omega}\|_{L^\infty}$ grows rapidly in the initial stage, it eventually slows down and starts to decrease, and the

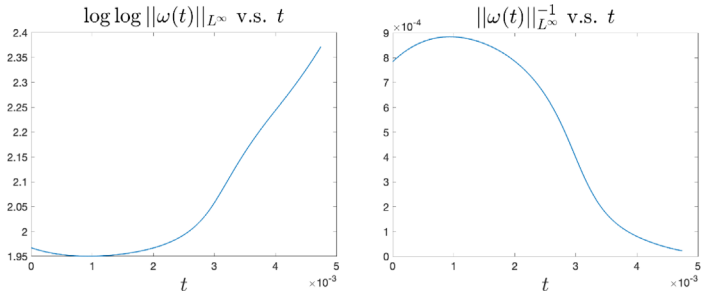

FIG. 25. *Evidence of non-blow-up for* $\alpha = 0.31$ *in* $\mathbb{R}^3$.

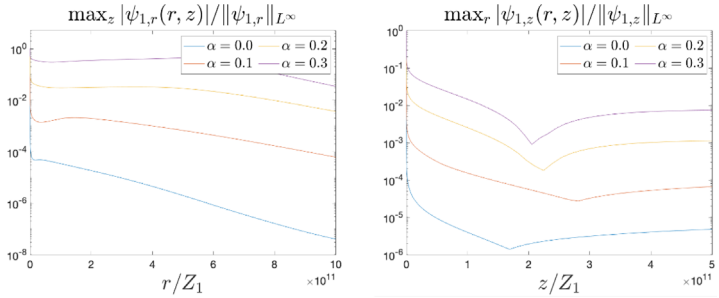

FIG. 26. *Decay of the derivatives of* ψ_1 *with different* α.

dynamic rescaling formulation fails to converge to a steady state. For example, in the case of $\alpha = 0.31$ shown in Figure 25, the double logarithm of $\|\omega\|_{L^\infty}$ becomes sublinear in the late stage, and $\|\omega\|_{L^\infty}^{-1}$ seems to decay slowly to zero, which would violate the BKM blow-up criterion. While the value $\alpha = 0.31$ is still far from the critical case of $\alpha = 1/3$, we remark that this could be due to the fact that the stability of the steady states becomes weaker as α tends to the critical value α^*. The largest real part of the eigenvalues of the Jacobian matrix, like we plotted in Figure 20, is -2.26 when $\alpha = 0.1$, -1.89 when $\alpha = 0.2$, and -0.53 when $\alpha = 0.3$. This shows that the steady states are less stable when α approaches α^*. Another reason is that $\tilde{c}_\omega + \alpha\tilde{c}_l$ is very close to zero as α tends to the critical value α^*. Thus, numerical errors may cause $\tilde{c}_\omega + \alpha\tilde{c}_l$ to change sign dynamically when α approaches α^*, which leads to non-blow-up. In order to capture the blow-up behavior as α approaches α^*, we need much higher resolution to prevent $\tilde{c}_\omega + \alpha\tilde{c}_l$ to change sign, which poses great numerical challenges in accuracy and computational time. We also note that the domain size D of the computational domain $\mathcal{D}'$ needs to be enlarged as α approaches the critical value α^*. In Figure 26, we plot the decay of derivatives of ψ_1 at the end of adaptive mesh method computation, which is also the starting point of the dynamic rescaling formulation computation. We can see that $\psi_{1,r}$ decays slower with a larger α, which implies that we need a larger domain size D to ensure that the zero Neumann boundary condition is appropriate. This further poses challenges in accuracy and computational time. Despite the numerical difficulty, the consistent potential blow-up behavior for $\alpha \le 0.3$ makes us believe that the 3D Euler equations could also develop potential self-similar blow-up for all $\alpha < 1/3$.

5.2. The dimension n. We extend the numerical study from the 3D case to the higher-dimensional case, and show that the critical value α^* is close to $1 - \frac{2}{n}$ in

the n-dimensional case. It is expected that the higher the dimension, the easier it is for a perfect fluid to form a singularity in finite time; see section 6 of [18]. We provide some numerical evidence to support such point of view.

In the n-dimensional case, we still use

$$u(x,t):\mathbb{R}^n\times[0,T)\to\mathbb{R}^n,\qquad\text{and}\qquad p(x,t):\mathbb{R}^n\times[0,T)\to\mathbb{R},$$

to denote the n-D vector field of the velocity and the n-D scalar field of the pressure, respectively, where $x=(x_1,x_2,\dots,x_n)\in\mathbb{R}^n$. Then the n-dimensional Euler equations can be written as

$$u_t+u\cdot\nabla u=-\nabla p, \tag{5.1a}$$

$$\nabla\cdot u=0. \tag{5.1b}$$

Next, we introduce $r=\sqrt{\sum_{k=1}^{n-1}x_k^2}$, $z=x_n$, and the unit vectors

$$e_r=(x_1/r,x_2/r,\dots,x_{n-1}/r,0),\qquad e_z=(0,0,\dots,0,1)\,.$$

Similar to the 3D case, we call an n-D vector field $v:\mathbb{R}^n\to\mathbb{R}^n$ to be axisymmetric and no swirl if the following ansatz applies:

$$v=v^r(r,z)e_r+v^z(r,z)e_z. \tag{5.2}$$

The axisymmetric n-D Euler equations with no swirl can be written in the vorticity-stream function form as

$$\omega_t^\theta+u^r\omega_r^\theta+u^z\omega_z^\theta=\frac{n-2}{r}u^r\omega^\theta, \tag{5.3a}$$

$$-\psi_{rr}^\theta-\psi_{zz}^\theta-\frac{n-2}{r}\psi_r^\theta+\frac{n-2}{r^2}\psi^\theta=\omega^\theta, \tag{5.3b}$$

$$u^r=-\psi_z^\theta,\quad u^z=\frac{n-2}{r}\psi^\theta+\psi_r^\theta, \tag{5.3c}$$

where we introduce the angular vorticity ω^θ and angular stream function ψ^θ as $\omega^\theta=u_z^r-u_r^z$ and $-\Delta\psi^\theta=\omega^\theta$, similar to the 3D axisymmetric Euler equations.

We would like to note that here we consider axisymmetric and no swirl condition together in (5.2) because if the velocity has component on a direction orthogonal to e_r and e_z, then the incompressibility condition $\nabla\cdot u=0$ will inevitably introduce dependence on variable other than r and z when the dimension n is greater than 3, even if this component only depends on r and z at time $t=0$.

Since we focus on C^α continuous initial data for the angular vorticity ω^θ, we introduce (ω_1,ψ_1) similarly as in (1.4), and rewrite the n-D axisymmetric Euler equations with no swirl in the below

$$\omega_{1,t}+u^r\omega_{1,r}+u^z\omega_{1,z}=-(n-2-\alpha)\psi_{1,z}\omega_1, \tag{5.4a}$$

$$-\psi_{1,rr}-\psi_{1,zz}-\frac{n}{r}\psi_{1,r}=\omega_1 r^{\alpha-1}, \tag{5.4b}$$

$$u^r=-r\psi_{1,z},\quad u^z=(n-1)\psi_1+r\psi_{1,r}. \tag{5.4c}$$

Roughly speaking, the dimension n controls the strength of the vortex stretching term $-(n-2-\alpha)\psi_{1,z}\omega_1$ and the velocity in the z-direction $u^z=(n-1)\psi_1+r\psi_{1,r}$. It also modifies the Poisson equation for ψ_1. It seems natural to conjecture that the singularity formation will be more likely in the high-dimensional case because of the stronger vortex stretching term $-(n-2-\alpha)\psi_{1,z}\omega_1$.

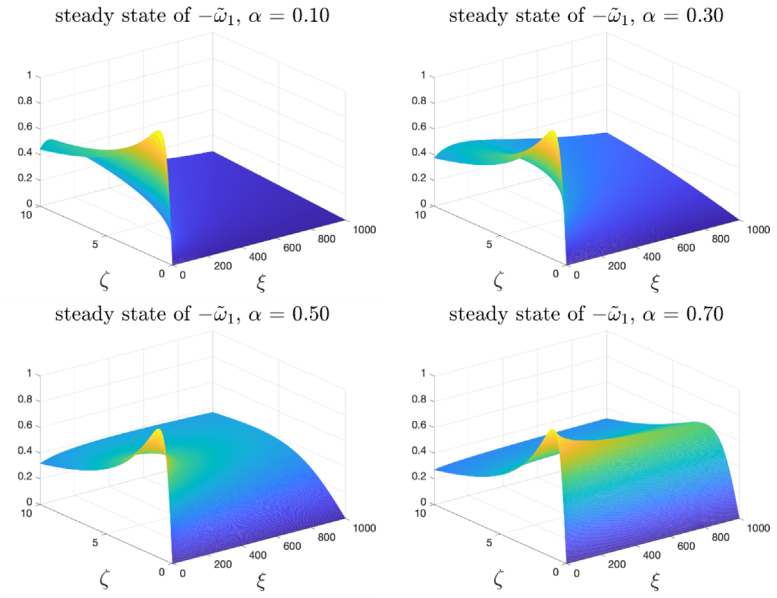

FIG. 27. *Steady states of* $-\tilde{\omega}_1$ *with different* α *in* $\mathbb{R}^{10}$.

In the following, for each combination of α and n, we first use the adaptive mesh method to solve (5.4) close enough to its possible blow-up time, and then use the dynamic rescaling formulation to continue the computation to capture the potential self-similar structure.

The steady states of $-\tilde{\omega}_1$ and $-\tilde{\psi}_1$ for $\alpha = 0.1, 0.3, 0.5, 0.7$ when the dimension $n = 10$ are plotted in Figure 27. In Figures 28 and 29, we provide the cross sections of the steady states $-\tilde{\omega}_1$ and $-\tilde{\psi}_1$ for different α when $n = 10$. Similar to the $n = 3$ case, we see that as α increases, the steady state becomes flatter in ξ. The cross section in ζ shows the different decay rates for different values of α. It is also very interesting to see that the ζ-cross section of $-\tilde{\psi}_1$ seems to be well approximated by a linear function of ζ in the near field.

In Table 5, we showed how c_l grows with α when $n = 10$. Similar to the observation in section 5.1, we see c_l quickly increases with α, and has the trend to go to infinity as α approaches α^*. We remark that in our computation, we found $\alpha^* > 0.72$. As in the 3D case in section 5.1, we need to solve the dynamic rescaling formulation on a larger computational domain with higher accuracy and longer physical time to reach the steady states for larger α. Based on our observation in the $n = 3$ case and $n = 10$ case, we conjecture that for our example, the critical value $\alpha^* = 1 - \frac{2}{n}$, which means our example would potentially support Conjecture 8 of [18] and extend it to the n-dimensional case.

We next study how the dimension n influences the finite-time blow-up. We fix $\alpha = 0.1$ and try different choices of dimensions $n = 3, 4, 5, 6, 8, 10$ using the same initial data

$$\omega_1^\circ = \frac{-12000\left(1 - r^2\right)^{18} \sin(2\pi z)}{1 + 12.5 \sin^2(\pi z)}.$$

We note that this initial data will lead to the same steady state phenomenon as the initial data in (2.5), as we will study in detail in section 6. We choose to report results in the n-dimensional case on this initial data because it takes less time to develop a

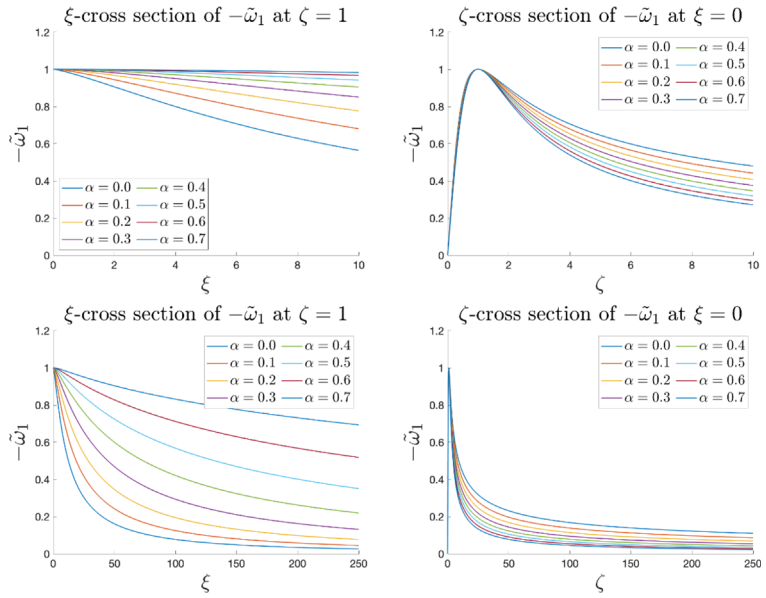

FIG. 28. *Cross sections of steady states of* $-\tilde{\omega}_1$ *with different* α *in* $\mathbb{R}^{10}$. *Top row: On a local window. Bottom row: On a larger window.*

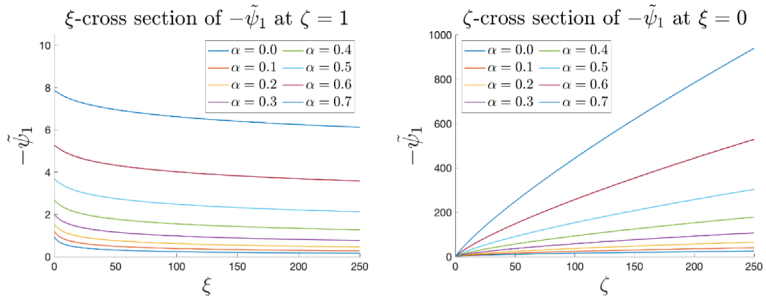

FIG. 29. *Cross sections of steady states of* $-\tilde{\psi}_1$ *with different* α *in* $\mathbb{R}^{10}$.

TABLE 5
The scaling factor c_l *with different* α *in the* n*-D case, where* $n = 10$.

α	0.0	0.1	0.2	0.3	0.4	0.5	0.6	0.7
c_l	2.155	2.432	2.811	3.363	4.244	5.897	10.16	47.14

potential blow-up, since the initial vorticity concentrates more near the origin, which helps reduce our computational cost.

In Table 6, we report the estimated blow-up times T and scaling factors c_l for different dimensions. It is not surprising that the blow-up time of the same initial data is shorter for the higher-dimensional case, because the vortex stretching term has a larger amplification coefficient. However, the scaling factor c_l is smaller for larger n. Intuitively, the velocity component u^z seems to be stronger with larger n. This phenomenon suggests that in the high-dimensional case, the dimension-related term $-\frac{n}{r}\partial_r$ in the Poisson equation controls ψ_1 and therefore weakens the collapsing speed of the solution. We also remark that the decay of c_l with n significantly slows down in Table 6. It is tempting to speculate if there is a limit of c_l as n approaches infinity.

TABLE 6
Estimated blow-up times T and scaling factors c_l in different dimensions with $\alpha = 0.1$.

n	3	4	5	6	8	10
$10^4 \times T$	4.183	3.589	2.877	2.498	2.089	1.866
c_l	4.549	3.218	2.851	2.680	2.514	2.432

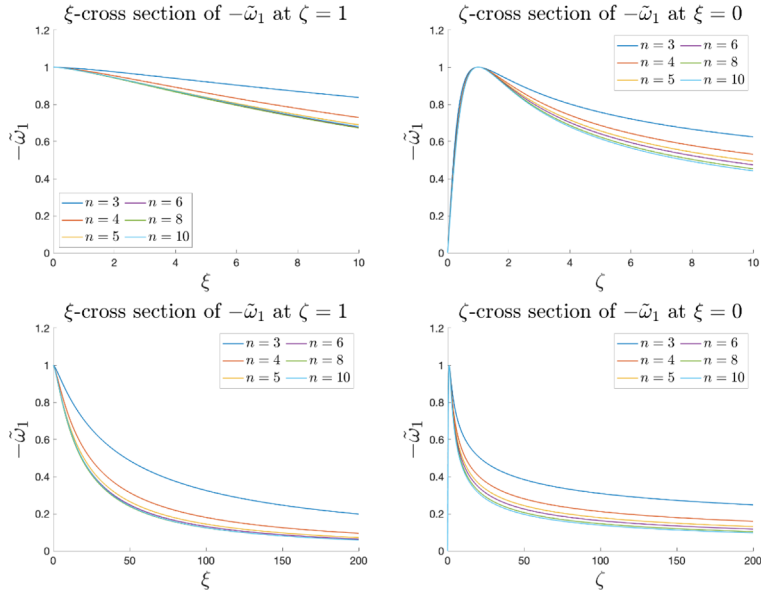

FIG. 30. *Cross sections of steady states of $-\tilde{\omega}_1$ with different n with $\alpha = 0.1$. Top row: On a local window. Bottom row: On a larger window.*

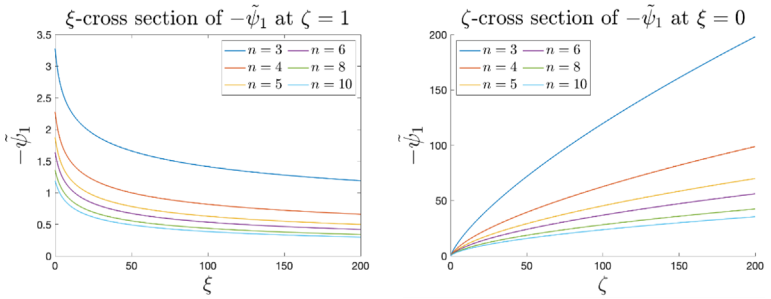

FIG. 31. *Cross sections of steady states of $-\tilde{\psi}_1$ with different n with $\alpha = 0.1$.*

In Figures 30 and 31, we provide the cross sections of the steady states of $-\tilde{\omega}_1$ and $-\tilde{\psi}_1$ from the dynamic rescaling formulation. We observe that the cross sections change with n. But as n becomes larger than 5, the difference quickly narrows down. This would give more evidence that there is some nontrivial limit as n goes to infinity. It would be very interesting to further explore this infinite dimension limit in the future.

6. Sensitivity of the potential blow-up to initial data. We study the sensitivity of the potential self-similar blow-up to initial data. In addition to the initial data (2.5), we consider the following cases:

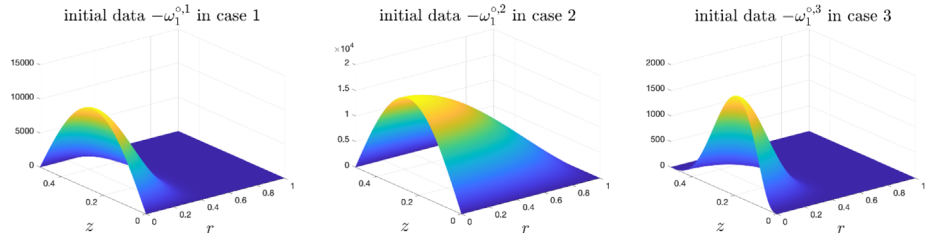

FIG. 32. *Profiles of the initial data in all three cases.*

$$
\begin{aligned}
\omega_1^{\circ,1} &= \frac{-12000\left(1-r^2\right)^{18}\sin(2\pi z)}{1+12.5\sin^2(\pi z)},\\
\omega_1^{\circ,2} &= -6000\cos\left(\frac{\pi r}{2}\right)\sin(2\pi z)\left(2+\exp\left(-r^2\sin^2(\pi z)\right)\right),\\
\omega_1^{\circ,3} &= \frac{-12000\left(1-r^2\right)^{18}\sin(2\pi z)^3}{1+12.5\sin^2(\pi z)}.
\end{aligned}
\tag{6.1}
$$

We show the profiles of these three initial data in Figure 32. In case 1, $\omega_1^{\circ,1}$ is a perturbation of ω_1° by setting cosine in the denominator to be sine, which is adopted as the initial data for the n-D case in section 5.2. In case 2, $\omega_1^{\circ,2}$ has a decay rate in r slower than $\left(1-r^2\right)^{18}$, and is no longer a simple tensor product of r and z. In case 3, $\omega_1^{\circ,3}$ has an improved regularity in $\rho=\sqrt{r^2+z^2}$ near the origin. Indeed, we have, with $\omega_1(r,z,0)=\omega_1^{\circ,3}(r,z)$,

$$\omega^\theta(r,z,0)=r^\alpha\omega_1^{\circ,3}(r,z)\sim r^\alpha z^3=\rho^{3+\alpha}\cos^\alpha\theta\sin^3\theta.$$

While for the original choice of the initial data (2.5), $\omega^\theta(r,z,0)\sim\rho^{1+\alpha}\cos^\alpha\theta\sin\theta$.

For all three cases, we only solve the 3D axisymmetric Euler equations with $\alpha=0.3$, due to the limited computational resources. As shown in Table 4, for our original initial data, $c_l=112.8$ is very large, which suggests that our choice of α is very close to the borderline between the blow-up and non-blow-up. If the blow-up profile of the above initial data agrees with our original initial data well, we then have good confidence that they should have the same behavior for other settings of α.

We solve the 3D axisymmetric Euler equations with the above initial data by first using the adaptive mesh method to get close enough to the potential blow-up time, and then using the dynamic rescaling method to capture the potential self-similar solution.

6.1. The first two cases: Same regularity near the origin. For the first and second cases, we show the fitting of $1/\|\omega\|_{L^\infty}$ with time t in Figure 33, and the curve of the scaling factor c_l in Figure 34. We can see that in both cases, $\|\omega\|_{L^\infty}$ scales like $1/(T-t)$, which implies a finite-time blow-up. Moreover, c_l converges to 112.8, matching the value of c_l we obtained using the original initial data well. In Figure 35, we show the cross sections of the steady state of $-\tilde{\omega}_1$ in comparison with the result obtained using the original initial data. There is no visible difference between the three steady states presented. In fact, even on the whole computational domain $\mathcal{D}'=\left\{(\xi,\zeta):0\le\xi\le1\times10^5,0\le\zeta\le5\times10^4\right\}$ in the dynamic rescaling computation, the steady states in the first and second cases only differ by 3.13×10^{-10} and 5.29×10^{-10}, respectively from the steady state using our original initial data ω_1° in the relative sup-norm.

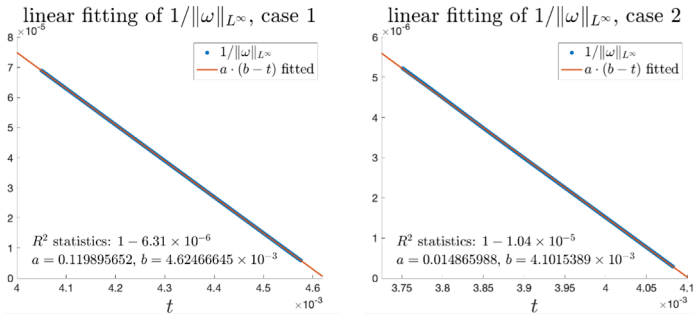

FIG. 33. *Fitting of* $1/\|\omega\|_{L^\infty}$ *with time* t *in the first and second cases.*

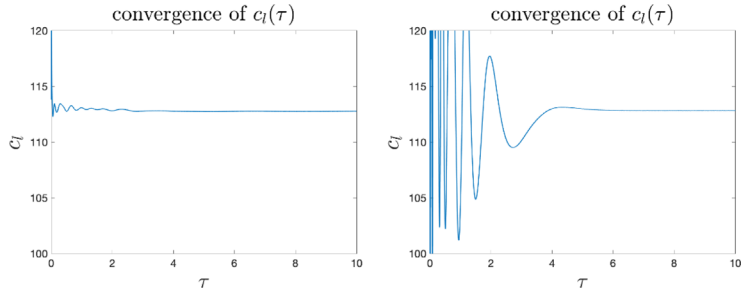

FIG. 34. *Curves of the scaling factor* c_l *in the first and second cases.*

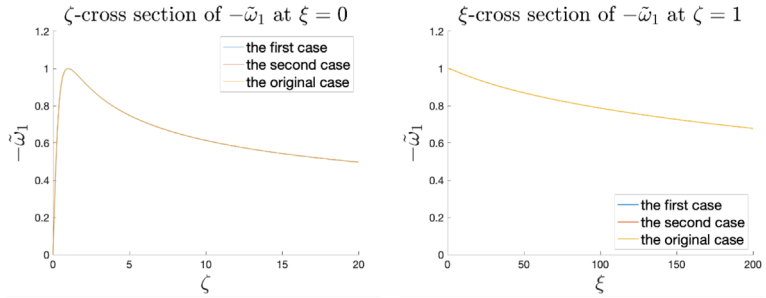

FIG. 35. *Cross sections of the steady states of* $-\tilde{\omega}_1$ *in the first and second cases.*

6.2. The third case: Improved regularity near the origin. For the third case, the fitting of $1/\|\omega\|_{L^\infty}$ and the curve of the scaling factor c_l is shown in Figure 36. We observe that $1/\|\omega\|_{L^\infty}$ has a good linear fitting with time, suggesting a finite-time blow-up. However, c_l converges to 19.44 which is clearly different from 112.8, suggesting that there might be a new blow-up mechanism. In Figure 37, we compare the steady states of $\omega_1^{\circ,3}$ and ω_1° in the 3D profiles and the 2D contours. The steady state of $\omega_1^{\circ,3}$ has a slower change near $z=0$. This might be caused by the smoothness of the initial data near $z=0$, because we have $\omega_1^{\circ,3}\sim r^\alpha z^3$, in contrast to $\omega_1^{\circ}\sim r^\alpha z$ near $(r,z)=(0,0)$. The steady state of the third case develops a channel-like structure that is not parallel to either axis.

The new blow-up scenario in the third case provides some support of Conjecture 9 of [18], in which the authors conjectured that the 3D Euler equations could still develop a finite-time blow-up for initial data that are C^∞ in ρ. In our future study, we plan to investigate the potential blow-up using a class of initial data of the form

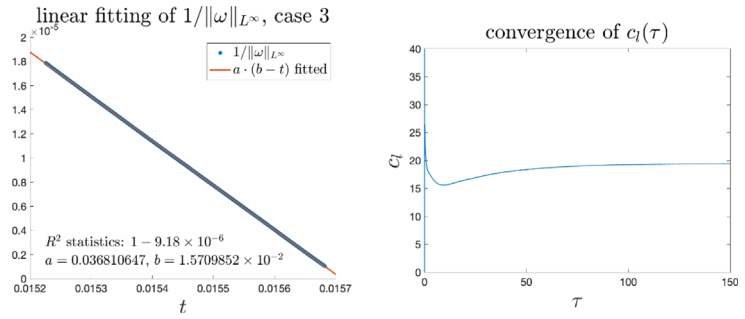

FIG. 36. *Fitting of* $1/\|\omega\|_{L^\infty}$ *and curve of the scaling factor* c_l *in the third case.*

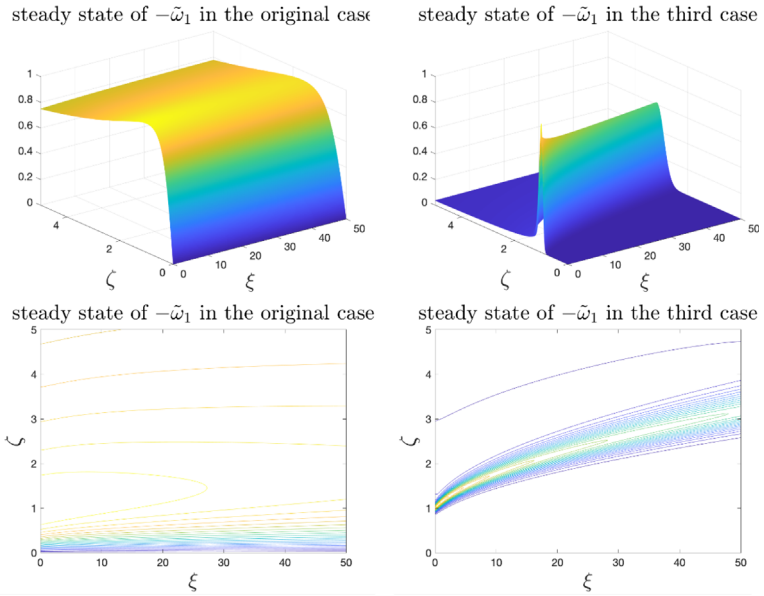

FIG. 37. *Profiles and contours of the steady states of* $-\tilde{\omega}_1$ *in the original and third cases.*

$$\omega_1^{\circ,4} = -12000\left(1-r^2\right)^{18}\sin(2\pi z)^{2k+1},$$

with a positive integer k, so that $\omega_1^{\circ,4} \sim r^\alpha z^{2k+1} = \rho^{2k+1+\alpha}\cos^\alpha\theta\sin^{2k+1}\theta$ is C^{2k+1} in ρ.

7. Comparison with Eligindi's singularity. In this section, we compare our blow-up scenario with the scenario in [20] studied by Elgindi.

Elgindi introduced a polar coordinate system on the (r,z)-plane to construct his blow-up solution. More specifically, he introduced

$$\rho = \sqrt{r^2+z^2}, \quad \theta = \arctan\left(\frac{z}{r}\right).$$

Then for a Hölder exponent α, he introduced a change of variable $R = \rho^\alpha$ and defined the variables

$$\Omega(R,\theta) = \omega^\theta(r,z), \quad \Psi(R,\theta) = \frac{1}{\rho^2}\psi^\theta(r,z).$$

In this setting, (1.3) can be rewritten as

(7.1a)
$$\Omega_t + (3\Psi + \alpha R\Psi_R)\,\Omega_\theta - (\Psi_\theta - \Psi\tan\theta)\,\Omega_R = (2\Psi\tan\theta + \alpha R\Psi_R\tan\theta + \Psi_\theta)\,\Omega,$$

(7.1b)
$$-\alpha^2 R^2\Psi_{RR} - \alpha(5+\alpha)R\Psi_R - \Psi_{\theta\theta} + (\Psi\tan\theta)_\theta - 6\Psi = \Omega.$$

Elgindi's analysis of (7.1b) establishes the following leading order approximation for small α:

$$\Psi(R,\theta) = \frac{1}{4\alpha}\sin(2\theta)L_{12}(\Omega)(R) + \text{lower order terms}, \tag{7.2}$$

where

$$L_{12}(\Omega)(R) = \int_R^\infty \int_0^{\frac{\pi}{2}} \Omega(s,\theta)\frac{K(\theta)}{s}\mathrm{d}s\mathrm{d}\theta,$$

with $K(\theta) = 3\sin\theta\cos^2\theta$. If we plug in the approximation (7.2) to (7.1a), neglecting lower order terms of α, and (time) scaling out some constant factor, we arrive at Elgindi's fundamental model

$$\Omega_t = \frac{1}{\alpha}L_{12}(\Omega)\Omega, \tag{7.3}$$

which admits self-similar finite-time blow-up. In his analysis, Elgindi chose the following self-similar solution of the fundamental model (7.3):

$$\Omega(R,\theta,t) = \frac{c}{1-t}F\left(\frac{R}{1-t}\right)\left(\sin\theta\cos^2\theta\right)^{\alpha/3}, \tag{7.4}$$

where $c>0$ is some fixed constant, and $F(z) = 2z/(1+z)^2$.

One difference between our blow-up scenario and Engindi's blow-up scenario is how the scaling factor c_l depends on α. We rewrite (7.4) as

$$\Omega = \frac{c}{1-t}F\left(\frac{\rho^\alpha}{1-t}\right)\left(\frac{r^2 z}{\rho^3}\right)^{\alpha/3} = \frac{c}{1-t}F\left(\left(\frac{\rho}{(1-t)^{1/\alpha}}\right)^\alpha\right)\left(\frac{r^{2/3}z^{1/3}}{\rho}\right)^\alpha.$$

If we let $G(z) = F(z^\alpha)$, we see

$$\Omega = \frac{c}{1-t}G\left(\frac{\rho}{(1-t)^{1/\alpha}}\right)\left(\frac{r^{2/3}z^{1/3}}{\rho}\right)^\alpha.$$

Since $r^{2/3}z^{1/3}/\rho$ is homogeneous, we may conclude that the scaling factors for the self-similar blow-up solution (7.4) are

$$c_l = 1/\alpha, \quad c_\omega = 2.$$

Note that this also satisfies the relation $c_\omega = 1 + \alpha c_l$ in (2.8). This implies that c_l decreases as α increases, and c_l will tend to infinity as $\alpha \to 0$. However, as shown in Tables 4 and 5, our c_l increases as α increases. In the limit of $\alpha \to 0$, our solution is well behaved and we observed a finite value of the scaling factor c_l when $\alpha = 0$, as reported in Table 4, while Elgindi's case needs some renormalization and c_l tends

to infinity. The scaling factor c_l in our case goes to infinity when α approaches to the critical value α^* which is close to $1/3$.

Furthermore, the regularity of our initial data as a function of ρ is different from that of Elgindi's initial data. Around $(r,z)=(0,0)$, Elgindi's initial condition has the following leading order behavior:

$$\Omega \sim \rho^\alpha \left(\sin\theta\cos^2\theta\right)^{\alpha/3} = r^{2\alpha/3} z^{\alpha/3}.$$

However, our initial condition gives

$$\omega^\theta = r^\alpha \omega_1^\circ \sim r^\alpha z = \rho^{1+\alpha}\cos^\alpha\theta\sin\theta.$$

These two leading order scaling properties differ from each other in that

- Elgindi's initial condition of ω^θ has a C^α Hölder continuity in ρ, whereas ours is $C^{1,\alpha}$ in ρ,
- Elgindi's initial condition of ω^θ is Hölder continuous in both $z=0$ and $r=0$, whereas our initial condition is Hölder continuous in $r=0$ but smooth in z.

In Conjecture 8 of [18], the authors conjectured that the initial data could be C^∞ in ρ for finite-time blow-up of the 3D axisymmetric Euler equations with no swirl. Our initial data slightly improves the regularity of the initial data in ρ. In section 6.2, we also briefly explored the initial data with higher regularity in ρ.

In Lemma 4.33 of [18], the authors stated that the limiting equations at $\alpha=0$ of (7.1) can blow up in finite time for initial data of Ω that only has a C^α-Hölder continuity near $r=0$ for $\alpha<1/3$. Our study shows that the blow-up of the axisymmetric Euler equations does not require to have Hölder continuity of the initial vorticity along the z-direction. The essential driving force for the finite-time blow-up comes from the Hölder continuity of the initial vorticity along the r-direction.

8. A 1D model of the potential self-similar blow-up. From Figures 23 and 28 in section 5, we observe that as α approaches the critical value α^*, $-\tilde{\omega}_1$ will become very flat in ξ. This inspires us to conjecture that in the $\alpha\to\alpha^*$ limit, $-\tilde{\omega}_1$ will eventually become a function of ζ only in a relatively large domain. Based on this observation, we assume that

$$\omega_1(r,z)=\omega_1(0,z), \tag{8.1}$$

and derive a 1D model for the n-D Euler equations (5.4).

At $r=0$, the velocity fields (5.4c) become $u^r=0$, $u^z=(n-1)\psi_1$. Therefore, the vorticity equation (5.4a) becomes

$$\omega_{1,t}(0,z)+(n-1)\psi_1(0,z)\omega_{1,z}(0,z) = -(n-2-\alpha)\psi_{1,z}(0,z)\omega_1(0,z).$$

As for the Poisson equation (5.4b), we use the Green's function $G_{n,\alpha}(r,r',z,z')$ for the operator $L_{n,\alpha}=r^{1-\alpha}\left(-\partial_{rr}-\frac{n}{r}\partial_r-\partial_{zz}\right)$. We have

$$\begin{aligned}\psi_1(r,z) &= \int_{(r',z')\in\mathcal{D}} G_{n,\alpha}(r,r',z,z')\omega_1(r',z')\mathrm{d}r'\mathrm{d}z',\\ &= \int_{(r',z')\in\mathcal{D}} G_{n,\alpha}(r,r',z,z')\omega_1(0,z')\mathrm{d}r'\mathrm{d}z',\end{aligned}$$

and therefore,

$$\psi_1(0,z)=\int_0^{1/2} H_{n,\alpha}(z,z')\omega_1(0,z')\mathrm{d}z',$$

where

$$H_{n,\alpha}(z,z') = \int_0^1 G_{n,\alpha}(0,r',z,z')\mathrm{d}r'.$$

Putting these equations together, and omitting the r-coordinate when there is no ambiguity, we have the following closed system in one dimension: for $z \in [0,1/2]$, ω_1 and ψ_1 are functions of z whose evolution in time is governed by the equations

$$\omega_{1,t} + (n-1)\psi_1\omega_{1,z} = -(n-2-\alpha)\psi_{1,z}\omega_1, \tag{8.2a}$$

$$\psi_1 = T_{n,\alpha}\omega_1, \tag{8.2b}$$

where $T_{n,\alpha}$ is an integral transform with kernel function $H_{n,\alpha}$:

$$T_{n,\alpha}\omega_1 = \int_0^{1/2} H_{n,\alpha}(z,z')\omega_1(z')\mathrm{d}z'.$$

8.1. The kernel function $H_{n,\alpha}$. We look for a more explicit expression for the kernel $H_{n,\alpha}$.

Following the idea in [27], we view $-\partial_{rr} - \frac{n}{r}\partial_r - \partial_{zz}$ as the Laplacian operator in the $(n+2)$-dimensional space for axisymmetric functions. The fundamental solution for the $(n+2)$-dimensional Laplace equation is

$$\Phi_0(x) = \frac{\Gamma(n/2)}{4\pi^{n/2+1}}\frac{1}{|x|^n},$$

for $x \in \mathbb{R}^{n+2}$. Now, since we have zero Dirichlet boundary conditions at $r=1$, $z=0$, $z=1/2$, we can obtain the Green's function for the above equation by properly symmetrizing the fundamental solution of the Laplace equation, which gives us

$$\begin{aligned} G_{n,\alpha}(r,r',z,z') = \sum_{m\in\mathbb{Z}} \big(& G^\circ_{n,\alpha}(r,r',z+m,z') - G^\circ_{n,\alpha}(r,r',-z+m,z') \\ & - G^\circ_{n,\alpha}(1,rr',z+m,z') + G^\circ_{n,\alpha}(1,rr',-z+m,z') \big), \end{aligned}$$

where

$$G^\circ_{n,\alpha}(r,r',z,z') = C(n)\frac{r'^{n+\alpha-1}}{A^{n/2}}{}_2F_1\left(n/2,n/2,n,B\right),$$

with Γ being the Gamma function, ${}_2F_1$ being the Gauss hypergeometric function, and

$$A = (r+r')^2 + (z-z')^2, \quad B = 4rr'/A, \quad C(n) = \frac{2^{n-2}}{\pi}\frac{\Gamma(n/2)^2}{\Gamma(n)}.$$

In fact, it is easy to check that $G_{n,\alpha}$ satisfies the boundary conditions:

$$G_{n,\alpha}(1,r',z,z') = G_{n,\alpha}(r,r',0,z') = G_{n,\alpha}(r,r',1/2,z') = 0.$$

We notice that the Gaussian hypergeometric function ${}_2F_1$ has the property that ${}_2F_1(n/2,n/2,n,0) = 1$. Therefore, we know that

$$G^\circ_{n,\alpha}(0,r',z,z') = \frac{C(n)r'^{n+\alpha-1}}{\left(r'^2+(z-z')^2\right)^{n/2}}, \quad G^\circ_{n,\alpha}(1,0,z,z') = 0.$$

Therefore, we arrive at an expression for $H_{n,\alpha}$:

$$H_{n,\alpha}(z,z') = \int_0^1 G_{n,\alpha}(0,r',z,z')\mathrm{d}r'$$
$$= C(n)\int_0^1 \sum_{m\in\mathbb{Z}} \left(\frac{r^{n+\alpha-1}}{\left(r^2+(z+m-z')^2\right)^{n/2}} - \frac{r^{n+\alpha-1}}{\left(r^2+(z-m+z')^2\right)^{n/2}} \right) \mathrm{d}r.$$

From $H_{n,\alpha}$, we can also find the integral transform for $\psi_{1,z}$:

$$\psi_{1,z}(z) = \int_0^{1/2} \partial_z H_{n,\alpha}(z,z')\omega_1(z')\mathrm{d}z',$$

with

$$\partial_z H_{n,\alpha}(z,z')$$
$$= nC(n)\int_0^1 \sum_{m\in\mathbb{Z}} \left(\frac{r^{n+\alpha-1}(z+m-z')}{\left(r^2+(z+m-z')^2\right)^{n/2+1}} - \frac{r^{n+\alpha-1}(z-m+z')}{\left(r^2+(z-m+z')^2\right)^{n/2+1}} \right) \mathrm{d}r.$$

In Figures 38 and 39, we show the profiles of the kernel functions $H_{n,\alpha}$ and $\partial_z H_{n,\alpha}$ for various combinations of (n,α). Figure 38 shows that the smaller α will make $H_{n,\alpha}$ and $\partial_z H_{n,\alpha}$ larger in scale. And this corresponds to the fact that smaller α is easier to develop the blow-up. In Figure 39, we see that as the dimension n increases, the profile of $H_{n,\alpha}$ seems to become shorter and thinner, which makes the velocity component $u^z = (n-1)\psi_1$ smaller. This phenomenon is consistent with Table 6 where larger n tends to have a slower collapsing rate.

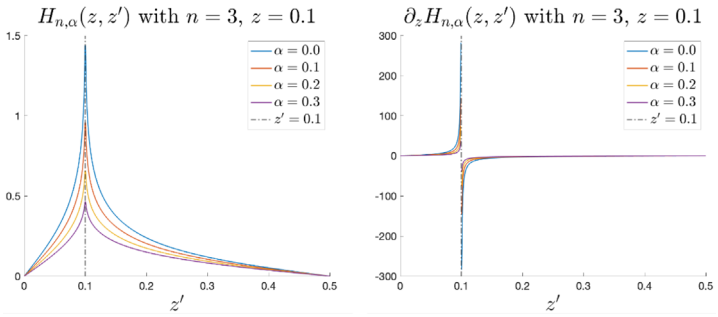

FIG. 38. *Profiles of $H_{n,\alpha}$ and $\partial_z H_{n,\alpha}$ as functions of z' for different α with $n=3$ and $z=0.1$.*

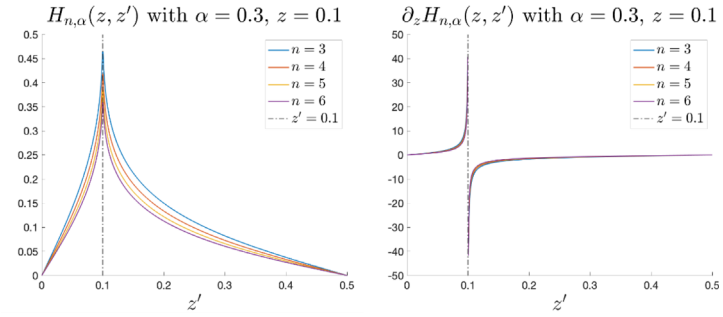

FIG. 39. *Profiles of $H_{n,\alpha}$ and $\partial_z H_{n,\alpha}$ as functions of z' for different n with $\alpha=0.3$ and $z=0.1$.*

8.2. Numerical simulation. Although the assumption (8.1) of our 1D model is based on our observation in the large α scenario, we simulate the 1D system (8.2) numerically with different choices of α to show its approximation to the n-D axisymmetric Euler equations (5.4).

Similar to our study in section 5.1, we use the adaptive mesh method to solve (8.2), and then compute the potential self-similar blow-up profile by solving the steady state of the following dynamic rescaling formulation:

$$\tilde{\omega}_{1,\tau} + \left(\tilde{c}_l\zeta + (n-1)\tilde{\psi}_1\right)\tilde{\omega}_{1,\zeta} = \left(\tilde{c}_\omega - (n-2-\alpha)\tilde{\psi}_{1,\zeta}\right)\tilde{\omega}_1, \tag{8.3a}$$

$$\tilde{\psi}_1 = T'_{n,\alpha}\tilde{\omega}_1. \tag{8.3b}$$

Here we use $T'_{n,\alpha}$ to distinguish from the integral transform $T_{n,\alpha}$ in (8.2), because $T'_{n,\alpha}$ is on the large domain $\mathcal{D}'$ with zero Neumann boundary condition in the far field, the same as the setup in section 4.2. In our computation, we use the late stage solution of (5.4) as the initial data to (8.2). To calculate the integral transform $T_{n,\alpha}$ numerically, we first temporarily lift up ω_1 from the 1D axis of z to the 2D plane of (r,z) by relation (8.1), then solve the Poisson equation (5.4b) on the (r,z)-plane for ψ_1, and finally restrict ψ_1 to the symmetry axis to obtain its value on the z-axis. The same method goes for the integral transform $T'_{n,\alpha}$, but on different computational domain ($\mathcal{D}'$) and with a different boundary condition in the far field.

Since the dimension n would not be critical in the comparison, we only consider the 3D case ($n=3$) here, with Hölder exponent $\alpha = 0.0, 0.1, 0.2, 0.3$. In Figure 40, we compare the steady state of $-\tilde{\omega}_1(0,\zeta)$ from the 3D axisymmetric Euler equations and the 1D model. When $\alpha = 0.3$, the two steady states match with each other quite well, with a relative sup-norm error of 1.5×10^{-3} on the ζ-axis. It is interesting to see that at small α, the two steady states are also close to each other. The relative sup-norm error at $\alpha = 0.0$ is smaller than 2.7×10^{-2} on the ζ-axis.

In Table 7, we report the comparison of the scaling factor c_l^{1D} of our 1D model and the scaling factor c_l for the 3D axisymmetric Euler equations. As α increases,

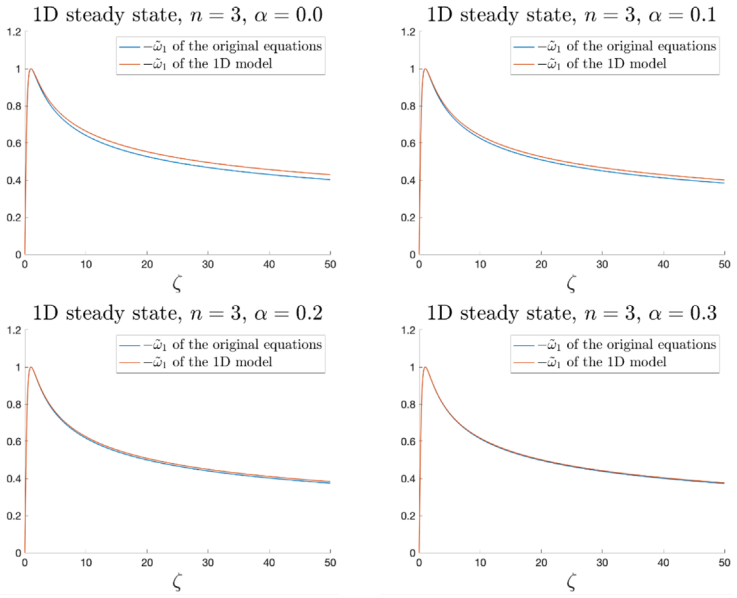

FIG. 40. *Comparison of the steady state of* $-\tilde{\omega}_1(0,\zeta)$ *with different* α.

TABLE 7
Scaling factor comparison between the 1D model and the 3D axisymmetric Euler equations.

α	0.0	0.1	0.2	0.3
c_l	3.248	4.549	8.270	112.8
$c_l^{1\mathrm{D}}$	3.374	4.682	8.464	114.8

the 1D model (8.2) can better approximate the 3D axisymmetric Euler equation in the relative error sense. This shows that our 1D model (8.2) can serve as a good model to understand the blow-up mechanism for the potential self-similar blow-up of the n-dimensional Euler equations. Although the 1D model is derived based on the flatness of ω_1 as a function of ξ as α is close to the critical value α^*, the agreement of c_l between the 1D model and the 3D Euler equations is still quite good for smaller values of α, which is quite surprising.

9. Concluding remarks. In this paper, we have numerically studied the singularity formation in the axisymmetric Euler equations with no swirl when the initial condition for the angular vorticity is C^α Hölder continuous. With carefully-chosen initial data and specially-designed adaptive mesh, we have solved the solution very close to the potential blow-up time, and obtained strong convincing numerical evidence for the singularity formation by numerically examining the BKM blow-up criterion. Scaling analysis and dynamic rescaling method have further suggested the potential self-similar blow-up. We observed the potential self-similar blow-up in finite time when the Hölder exponent α is greater than or equal to 0, and is smaller than a critical value α^*, and this upper bound α^* is larger than 0.3, and have the potential to be 1/3. This result supports Conjecture 8 of [18]. Since when $\alpha > 1/3$, the axisymmetric Euler equations with no swirl admit global regularity [54, 50, 51, 49, 16, 1], this would potentially close the gap between blow-up and non-blow-up, leaving only the critical case of $\alpha = 1/3$. We also extend this result to the high-dimensional case, and find that, in general, the critical value α^* for the n-D axisymmetric Euler equation is close to $1 - \frac{2}{n}$.

The potential blow-up observed in this paper is insensitive to the perturbation of initial data. And our initial study suggested that the regularity of the initial data around the origin would determine its scaling properties and the shape of the self-similar blow-up profile. Compared with Elgindi's blow-up result reported in [20], our potential blow-up scenario has very different scaling properties. The regularity properties of the initial condition of the two initial data are also quite different.

Inspired by our numerical observations, we proposed a simple 1D model to capture the leading order behavior of the n-dimensional Euler equations. Our numerical experiments showed that the 1D model can develop approximately the same potential finite-time blow-up as the original n-dimensional Euler equations. This 1D model could play a role similar to the leading order system derived by Elgindi in [20] in the analysis of the finite-time singularity of the 3D Euler equations.

Acknowledgments. We would like to thank Mr. Xiang Qin and Mr. Xiuyuan Wang from Peking University for helpful discussion.

REFERENCES

[1] H. ABIDI, T. HMIDI, AND S. KERAANI, *On the global well-posedness for the axisymmetric Euler equations*, Math. Ann., 347 (2010), pp. 15–41.
[2] J. T. BEALE, T. KATO, AND A. MAJDA, *Remarks on the breakdown of smooth solutions for the 3D Euler equations*, Comm. Math. Phys., 94 (1984), pp. 61–66.

[3] M. D. Bustamante and R. M. Kerr, *3D Euler about a 2D symmetry plane*, Phys. D, 237 (2008), pp. 1912–1920.
[4] R. E. Caflisch, *Singularity formation for complex solutions of the 3D incompressible Euler equations*, Phys. D, 67 (1993), pp. 1–18.
[5] J. Chen, *Remarks on the smoothness of the $C^{1,\alpha}$ asymptotically self-similar singularity in the 3D Euler and 2D Boussinesq equations*, Nonlinearity, 37 (2024), 065018.
[6] J. Chen and T. Y. Hou, *Finite time blowup of 2D Boussinesq and 3D Euler equations with $C^{1,\alpha}$ velocity and boundary*, Comm. Math. Phys., 383 (2021), pp. 1559–1667.
[7] J. Chen and T. Y. Hou, *Stable Nearly Self-Similar Blowup of the 2D Boussinesq and 3D Euler Equations with Smooth Data* I*: Analysis*, preprint, https://arxiv.org/abs/2210.07191, 2022.
[8] J. Chen and T. Y. Hou, *Stable Nearly Self-Similar Blowup of the 2D Boussinesq and 3D Euler Equations with Smooth Data* II*: Rigorous Numerics*, preprint, https://arxiv.org/abs/2305.05660, 2023.
[9] J. Chen, T. Y. Hou, and D. Huang, *On the finite time blowup of the De Gregorio model for the 3D Euler equations*, Comm. Pure Appl. Math., 74 (2021), pp. 1282–1350.
[10] J. Chen, T. Y. Hou, and D. Huang, *Asymptotically self-similar blowup of the Hou-Luo model for the 3D Euler equations*, Ann. PDE, 8 (2022), 24.
[11] K. Choi, T. Y. Hou, A. Kiselev, G. Luo, V. Sverak, and Y. Yao, *On the finite-time blowup of a one-dimensional model for the three-dimensional axisymmetric Euler equations*, Comm. Pure Appl. Math., 70 (2017), pp. 2218–2243.
[12] K. Choi, I.-J. Jeong, and D. Lim, *Global Regularity for Some Axisymmetric Euler Flows in $\mathbb{R}^d$*, preprint, https://arxiv.org/abs/2212.11461, 2022.
[13] P. Constantin, C. Fefferman, and A. J. Majda, *Geometric constraints on potentially singular solutions for the 3D Euler equations*, Comm. Partial Differential Equations, 21 (1996), pp. 559–571.
[14] D. Córdoba and L. Martínez-Zoroa, *Blow-up for the Incompressible 3D-Euler Equations with Uniform $C^{1,\frac{1}{2}-\varepsilon}\cap L^2$ Force*, preprint, https://arxiv.org/abs/2309.08495, 2023.
[15] D. Córdoba, L. Martínez-Zoroa, and F. Zheng, *Finite Time Singularities to the 3D Incompressible Euler Equations for Solutions in $C^\infty(\mathbb{R}^3\setminus\{0\})\cap C^{1,\alpha}\cap L^2$*, preprint, https://arxiv.org/abs/2308.12197, 2023.
[16] R. Danchin, *Axisymmetric incompressible flows with bounded vorticity*, Russian Math. Surveys, 62 (2007), pp. 475–496.
[17] J. Deng, T. Y. Hou, and X. Yu, *Geometric properties and nonblowup of 3D incompressible Euler flow*, Comm. Partial Differential Equations, 30 (2005), pp. 225–243.
[18] T. D. Drivas and T. M. Elgindi, *Singularity formation in the incompressible Euler equation in finite and infinite time*, EMS Surv. Math. Sci., 10 (2023), pp. 1–100.
[19] W. E and C.-W. Shu, *Numerical Study of the Small Scale Structures in Boussinesq Convection*, ICASE Report No. 92-40, 1992.
[20] T. M. Elgindi, *Finite-time singularity formation for $C^{1,\alpha}$ solutions to the incompressible Euler equations on $\mathbb{R}^3$*, Ann. of Math., 194 (2021), pp. 647–727.
[21] T. M. Elgindi and F. Pasqualotto, *From Instability to Singularity Formation in Incompressible Fluids*, preprint, https://arxiv.org/abs/2310.19780, 2023.
[22] C. L. Fefferman, *Existence and smoothness of the Navier-Stokes equation*, Millennium Prize Problems, Cambridge, 2000, pp. 57–67.
[23] A. B. Ferrari, *On the blow-up of solutions of the 3D Euler equations in a bounded domain*, Comm. Math. Phys., 155 (1993), pp. 277–294.
[24] J. D. Gibbon, *The three-dimensional Euler equations: Where do we stand?*, Phys. D, 237 (2008), pp. 1894–1904.
[25] R. Grauer and T. C. Sideris, *Numerical computation of 3D incompressible ideal fluids with swirl*, Phys. Rev. Lett., 67 (1991), 3511.
[26] T. Y. Hou, *Potentially singular behavior of the 3D Navier–Stokes equations*, Found. Comput. Math., 23 (2023), pp. 2251–2299.
[27] T. Y. Hou, T. Jin, and P. Liu, *Potential singularity for a family of models of the axisymmetric incompressible flow*, J. Nonlinear Sci., 28 (2018), pp. 2217–2247.
[28] T. Y. Hou and R. Li, *Dynamic depletion of vortex stretching and non-blowup of the 3D incompressible Euler equations*, J. Nonlinear Sci., 16 (2006), pp. 639–664.
[29] R. M. Kerr, *Evidence for a singularity of the three-dimensional, incompressible Euler equations*, Phys. Fluids A, 5 (1993), pp. 1725–1746.
[30] R. M. Kerr, *Bounds for Euler from vorticity moments and line divergence*, J. Fluid Mech., 729 (2013), R2.

[31] A. Kiselev, *Small scales and singularity formation in fluid dynamics*, in Proceedings of the International Congress of Mathematicians (ICM 2018), World Scientific, 2019, pp. 2363–2390.

[32] A. Kiselev, L. Ryzhik, Y. Yao, and A. Zlatoš, *Finite time singularity for the modified SQG patch equation*, Ann. of Math., 184 (2016), pp. 909–948.

[33] A. Kiselev and V. Šverák, *Small scale creation for solutions of the incompressible two-dimensional Euler equation*, Ann. of Math., 180 (2014), pp. 1205–1220.

[34] M. Landman, G. C. Papanicolaou, C. Sulem, P. L. Sulem, and X. P. Wang, *Stability of isotropic self-similar dynamics for scalar-wave collapse*, Phys. Rev. A, 46 (1992), pp. 7869–7876.

[35] M. J. Landman, G. C. Papanicolaou, C. Sulem, and P.-L. Sulem, *Rate of blowup for solutions of the nonlinear Schrödinger equation at critical dimension*, Phys. Rev. A, 38 (1988), pp. 3837–3843.

[36] B. J. LeMesurier, G. C. Papanicolaou, C. Sulem, and P. Sulem, *Focusing and multi-focusing solutions of the nonlinear Schrödinger equation*, Phys. D, 31 (1988), pp. 78–102.

[37] D. Lim, *Global Regularity for Some Axisymmetric, Single-Signed Vorticity in Any Dimension*, preprint, https://arxiv.org/abs/2304.12089, 2023.

[38] J.-G. Liu and W.-C. Wang, *Convergence analysis of the energy and helicity preserving scheme for axisymmetric flows*, SIAM J. Numer. Anal., 44 (2006), pp. 2456–2480, https://doi.org/10.1137/050639314.

[39] J.-G. Liu and W.-C. Wang, *Characterization and regularity for axisymmetric solenoidal vector fields with application to Navier–Stokes equation*, SIAM J. Math. Anal., 41 (2009), pp. 1825–1850, https://doi.org/10.1137/080739744.

[40] P. Liu, *Spatial Profiles in the Singular Solutions of the 3D Euler Equations and Simplified Models*, Ph.D. thesis, California Institute of Technology, Pasadena, CA, 2017.

[41] G. Luo and T. Y. Hou, *Potentially singular solutions of the 3D axisymmetric Euler equations*, Proc. Natl. Acad. Sci. USA, 111 (2014), pp. 12968–12973.

[42] G. Luo and T. Y. Hou, *Toward the finite-time blowup of the 3D axisymmetric Euler equations: A numerical investigation*, Multiscale Model. Simul., 12 (2014), pp. 1722–1776, https://doi.org/10.1137/140966411.

[43] G. Luo and T. Y. Hou, *Formation of finite-time singularities in the 3D axisymmetric Euler equations: A numerics guided study*, SIAM Rev., 61 (2019), pp. 793–835, https://doi.org/10.1137/19M1288061.

[44] A. J. Majda and A. L. Bertozzi, *Vorticity and Incompressible Flow*, Vol. 27, Cambridge University Press, 2002.

[45] D. W. McLaughlin, G. C. Papanicolaou, C. Sulem, and P.-L. Sulem, *Focusing singularity of the cubic Schrödinger equation*, Phys. Rev. A, 34 (1986), pp. 1200–1210.

[46] E. Miller, *On the Regularity of Axisymmetric, Swirl-Free Solutions of the Euler Equation in Four and Higher Dimensions*, preprint, https://arxiv.org/abs/2204.13406, 2022.

[47] G. C. Papanicolaou, C. Sulem, P. L. Sulem, and X. P. Wang, *The focusing singularity of the Davey-Stewartson equations for gravity-capillary surface waves*, Phys. D, 72 (1994), pp. 61–86.

[48] A. Pumir and E. D. Siggia, *Development of singular solutions to the axisymmetric Euler equations*, Phys. Fluids, 4 (1992), pp. 1472–1491.

[49] X. Saint Raymond, *Remarks on axisymmetric solutions of the incompressible Euler system*, Comm. Partial Differential Equations, 19 (1994), pp. 321–334.

[50] P. Serfati, *Régularité stratifiée et équation d'Euler 3Da temps grand*, C. R. Acad. Sci. Paris Sér. I Math., 318 (1994), pp. 925–928.

[51] T. Shirota and T. Yanagisawa, *Note on global existence for axially symmetric solutions of the Euler system*, Proc. Japan Acad. Ser. A Math. Sci., 70 (1994), pp. 299–304.

[52] M. Siegel and R. E. Caflisch, *Calculation of complex singular solutions to the 3D incompressible Euler equations*, Phys. D, 238 (2009), pp. 2368–2379.

[53] G. Strang, *On the construction and comparison of difference schemes*, SIAM J. Numer. Anal., 5 (1968), pp. 506–517, https://doi.org/10.1137/0705041.

[54] M. Ukhovskii and V. Iudovich, *Axially symmetric flows of ideal and viscous fluids filling the whole space*, J. Appl. Math. Mech., 32 (1968), pp. 52–61.

[55] S. Zhang, *Singularity Formation in the High-Dimensional Euler Equations and Sampling of High-Dimensional Distributions by Deep Generative Networks*, Ph.D. thesis, California Institute of Technology, Pasadena, CA, 2023.